TECHNISCHE UNIVERSITÄT WIEN
Vienna University of Technology

Diplomarbeit

Homoepitaxial Growth Experiments of $SrTiO_3(110)$

ausgeführt am Institut für Angewandte Physik
der Technischen Universität Wien

unter der Anleitung von
Univ.Prof. Dipl.-Ing. Dr.techn. Ulrike DIEBOLD,
Dr. Michele RIVA
und
Dott.mag. Giada FRANCESCHI

durch

Sebastian MOSER, BSc.
Matr.Nr.: 01227150

Februar, 2018

Kurzfassung

Mittels Laserstrahlverdampfens wurde eine Reihe homoepitaktischer Schichtwachstumsexperimente von $SrTiO_3(110)$ durchgeführt, die durch unterschiedliche Energieflussdichten des Ablationslasers charakterisiert waren. Sowohl die sorgfältig präparierten $SrTiO_3(110)$ Substrate, die durch die Koexistenz von (4×1) und (5×1) Oberflächenrekonstruktionen geprägt waren, als auch die aufgewachsenen Schichten wurden durch verschiedene oberflächensensible Analysetechniken in Vakuumumgebung untersucht. Dazu zählten Beugung niederenergetischer Elektronen an Oberflächen (*low-energy electron diffraction*), Beugung hochenergetischer Elektronen bei Reflexion (*reflection high-energy electron diffraction*), Rastertunnelmikroskopie sowie Röntgenphotoelektronenspektroskopie. Um Abweichungen von der idealen Stöchiometrie beim Schichtwachstum zu quantifizieren, wurde eine innovative Methode etwickelt, die auf einer statistischen Auswertung der Rastertunnelmikroskopiebilder vor beziehungsweise nach dem Depositionsprozess beruht. Auf Basis dieser Methode wurde gezeigt, dass Schichten, die durch niedrige Energieflussdichten des Ablationslasers charakterisiert sind, Sr angereichert sind, während hohe Energieflussdichten zu einem Ti-Überschuss führen. Dieser ist jedoch signifikant geringer als der Sr-Überschuss in mit geringen Energieflussdichten aufgebrachten Schichten.

ABSTRACT

Pulsed laser deposition was used to perform a series of homoepitaxial growth experiments of $SrTiO_3(110)$ characterized by different fluences of the ablation laser. The well-prepared (4×1)-(5×1)-reconstructed $SrTiO_3(110)$ substrates, as well as the grown films were analysed by several *in-situ* surface sensitive techniques, comprising low-energy electron diffration, reflection high-energy electron diffraction, scanning tunnelling microscopy, and X-ray photoelectron spectroscopy. In order to perform a precise quantification of off-stoichiometries within the growth processes, an innovative method, based on a statistical evaluation of scanning tunnelling microscopy images before and after the deposition processes, was developed. Based on this method, it was shown that films grown using low fluences are characterized by a Sr-enrichment, while high fluences lead to a Ti enrichment, which is, however, significantly lower compared to the Sr-excess present in films deposited with low fluences.

Contents

1 INTRODUCTION

Strontium titanate ($SrTiO_3$, STO) has attracted significant interest in different fields of scientific research due to its remarkable electronic properties and photocatalytic reactivity [1, 2]. These properties can also be selectively tuned by introducing dopants or by finely adjusting the stoichiometry, *e.g.* by introducing oxygen vacancies [3, 4]. A very prominent example showcasing the possibilities of such functional tailoring is the heterointerface between $LaTiO_3$ and $SrTiO_3$. Even though both materials are insulators, the interface shows metallic character (two dimensional electron gas) depending on the atomic termination of the interlayer [5]. In later studies even superconductivity was measured at this particular interface [6].

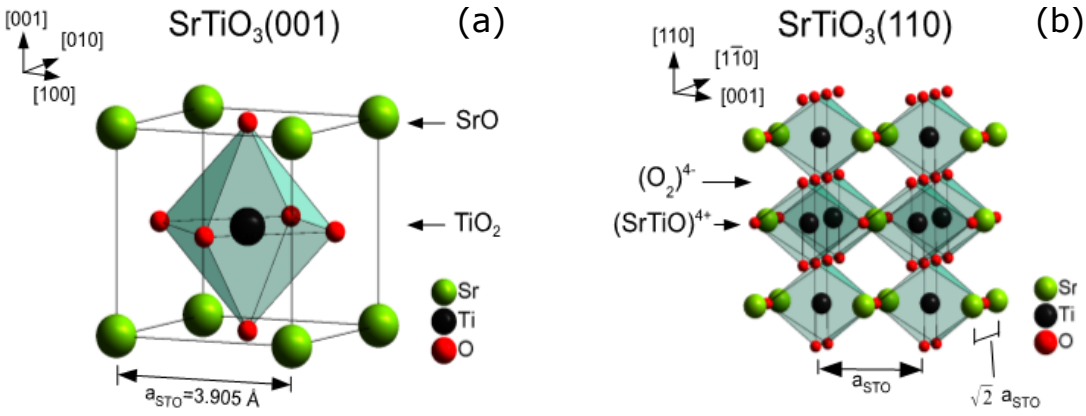

FIGURE 1.1: (a) STO unit cell. (b) Layer stacking of STO along [110].

A schematic representation of the STO unit cell is displayed in Figure 1.1(a). The cell is characterized by a cubic structure with a lattice constant of $a = 3.905$ Å. Sr-atoms are located at the corners, while an octahedrally coordinated Ti-atom is located in the body center, and is bound to the six oxygen-atoms at the face centers. As shown in Figure 1.1(b), along the [110] direction STO is composed of alternatively stacked atomic layers of $(SrTiO)^{4+}$ and $(O_2)^{4-}$, and therefore the ideal bulk truncated STO(110) surface would be characterized by a macroscopic electric dipole moment [7]. In real STO(110) crystals, however, such a dipole moment is

compensated by the formation of a series of different surface reconstructions [not shown in Figure 1.1(b)], allowing to minimize the surface energy.

The STO(110) surface phase diagram in Figure 1.2 gives an overview of the different surface reconstructions, as observed by means of scanning tunnelling microscopy (STM) and low-energy electron diffraction (LEED); at the same time it provides information on how to transform reversibly one specific reconstruction to another, by depositing a well-defined amount of Ti or Sr, respectively, followed by thermal annealing in oxygen environment [8]. It has to be noted that the (6×1), (5×1), and (4×1) reconstructions, which are all characterized by stripes along the $[1\bar{1}0]$ direction, belong to a generalized series of structures, referred to as $(n\times1)$, which is well understood from a theoretical point of view [9].

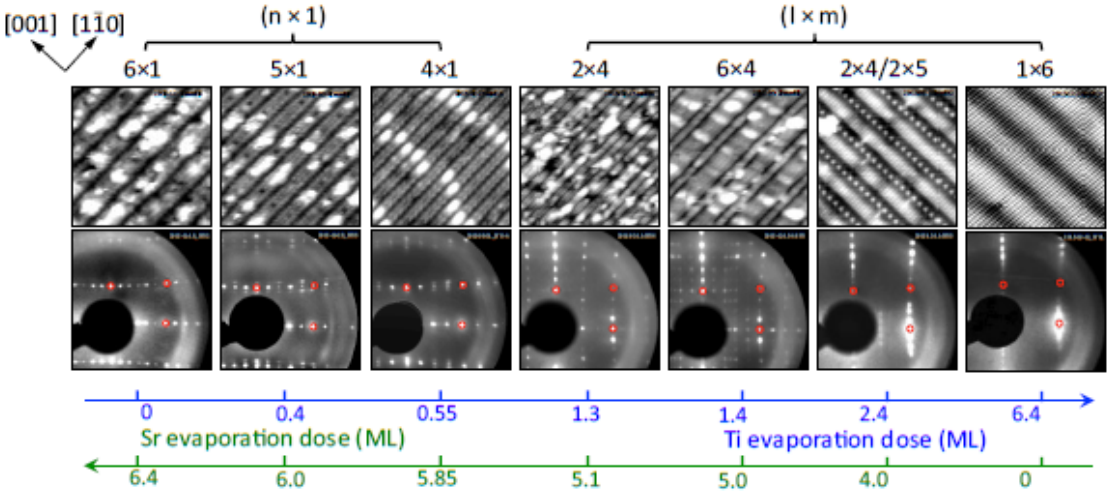

FIGURE 1.2: Surface phase diagram of STO(110). The first row exhibits small-scale STM images of the different types of surface reconstructions and the second row shows their corresponding LEED patterns using 90 eV electrons. The spots corresponding to the bulk unit cell are highlighted by the red circles. The axes show the amount of Sr and Ti that has to be deposited to tune the surface from one specific reconstruction to another. This image is reprinted from [10]. The calibration of the deposition amounts was performed by [11].

Within the past decades pulsed laser deposition (PLD) has been proven to be one of the best techniques to grow high-quality films of complex oxides [12, 13]. By optimizing the process parameters it is possible to achieve stoichiometric growths, here using a specific value of the ablation laser fluence plays an important role [14, 15]. It is important to achieve such precise growth conditions because even small deviations in the stoichiometry of complex oxides, such as STO, can lead to significant changes in their electronic properties [16]. However, such optimized growth parameters are usually corresponding to one particular PLD setup.

The objective of this thesis was to grow homoepitaxial films of STO(110) by means of PLD, and to optimize the fluence of the ablation laser used within this process, such that stoichiometric results were obtained. At the same time an innovative, STM-based method for quantification of the off-stoichiometries in homoepitaxial films of STO(110) was developed and put into practice. This particular method is strongly based on results presented in surface phase diagram of STO(110) (see Figure 1.2), and it is shown to be significantly more accurate compared to X-ray photoelectron spectroscopy (XPS), X-ray diffraction (XRD), and transmission electron microscopy (TEM), which are commonly used to quantify off-stoichiometries within thin film growths.

2 GENERAL ASPECTS OF THE TECHNIQUES USED

This section provides a general overview and some theoretical aspects of the surface characterization techniques scanning tunnelling microscopy (STM), X-ray photoelectron spectroscopy (XPS), low-energy electron diffraction (LEED), and reflection high-energy electron diffraction (RHEED), which have been used within the experiments presented in this thesis. In order to keep the descriptions in a general context, it is explicitly avoided to use any numerical values for the operation parameters in this particular section, since they usually differ not only for different experimental setups, but also for different types of samples. In the description of the individual chambers in Chapter 3, and in the experimental part of this thesis the values of those parameters are well documented. The deposition techniques molecular beam epitaxy (MBE) and pulsed laser deposition (PLD) are also introduced in this section.

2.1 Scanning tunnelling microscopy - STM

STM is a technique used to study the surface topography of samples at the nanoscale. It provides direct, real-space images of surfaces. A nanoscopic tip scans a biased sample surface, while the tip-sample distance is adjusted in such a way that an electric tunnelling current in between them is kept constant. These adjustments are plotted in a 2D array. Alternatively, STM can also be operated in a constant height mode, in which the current is measured while scanning the tip without changing its height. Operating in this mode is only possible for small and perfectly-flat surface areas.

The fundamental principle of STM is based on the quantum mechanical tunnelling effect between a metallic tip and a conducting or semiconducting sample. The simplest model of the tunnelling effect is described by a one-dimensional potential

barrier, as schematically shown in Figure 2.1(a) and (b). Within this model just electrons at the Fermi energy are considered, and it is assumed that the potential barrier is rectangularly shaped with a width d, which corresponds to the distance between tip and sample, and a height $\phi = \frac{1}{2}(\phi_{\text{tip}}+\phi_{\text{sample}})$, defined by the averaged work function of tip and sample, respectively.

In order to study the physics of such a system, one has to solve the time-independent Schrödinger's equation for the as-described potential $V(z)$, summarized in Equation 2.1, where $\hbar$ is the reduced Planck's constant, m is the rest mass of an electron, $\Psi(z)$ is the wave function and E is the energy of the electrons. The solution is described by plane waves in the tip ($z < z_0$) and the sample ($z > z_0$+d) regions, and by an exponentially decaying wave function in between, as described in Equation 2.2. The tunnelling current is proportional to the transmission, which subsequently is proportional to an exponential function of the tip-sample distance d. This is a fundamental result, and experiments have shown that the tunnelling current follows such a characteristic law for 3D geometries as well.

There is no doubt that in a more realistic model of an STM one has to take other parameters and properties into consideration as well. (1) The local densities of electronic states of the tip and the sample have to be taken into account. (2) There is a tunnelling voltage U_{t} applied between tip and sample, which causes a shift in the Fermi energies and may cause a net tunnelling current between tip and sample. The influence of these two aspects is illustrated by Figure 2.1(c): There is a metallic tip and a semiconducting sample, which is positively biased by the voltage U_{t}, causing a shift in the Fermi energies of tip and sample. Filled states are coloured dark gray in the electronic density of states (DOS) curves whereas empty states are white. The yellow coloured area in the the DOS curve of the sample represents empty states, which can potentially be filled by tunnelling electrons from the tip. As a conclusion, it follows that the tunnelling current not only depends on the tip-sample distance, but also on the local density of electric states of the tip and sample. In case the sample is positively/negatively biased with respect to the tip, empty/filled states of the sample are probed.

A simplified realization of the scanning mechanism of an STM is shown in Figure 2.1(d). The tip is attached on a piezoelectric scanning device, represented by the big cylindrical object in Figure 2.1(d). By applying a voltage, U_y between the side electrodes facing the $+y$ and $-y$ directions, the scanner will be deformed along this axis due to its piezoelectric properties, resulting in a corresponding movement

of the tip in that direction. By applying time-dependent voltages U_x and U_y simultaneously, a planar movement can be achieved, which can be used to scan the sample surface. Finally, U_z is continuously regulated by the distance control unit in such a way that the set tunnelling current, I_t, stays constant during the scanning process. The required change in height is recorded as a function of x and y, and can be displayed as a gray-scale image on the computer. Due to the fact that the movements involved are in the nanometer range, it is required to have an excellent vibration damping system to isolate the STM apparatus from external influences.

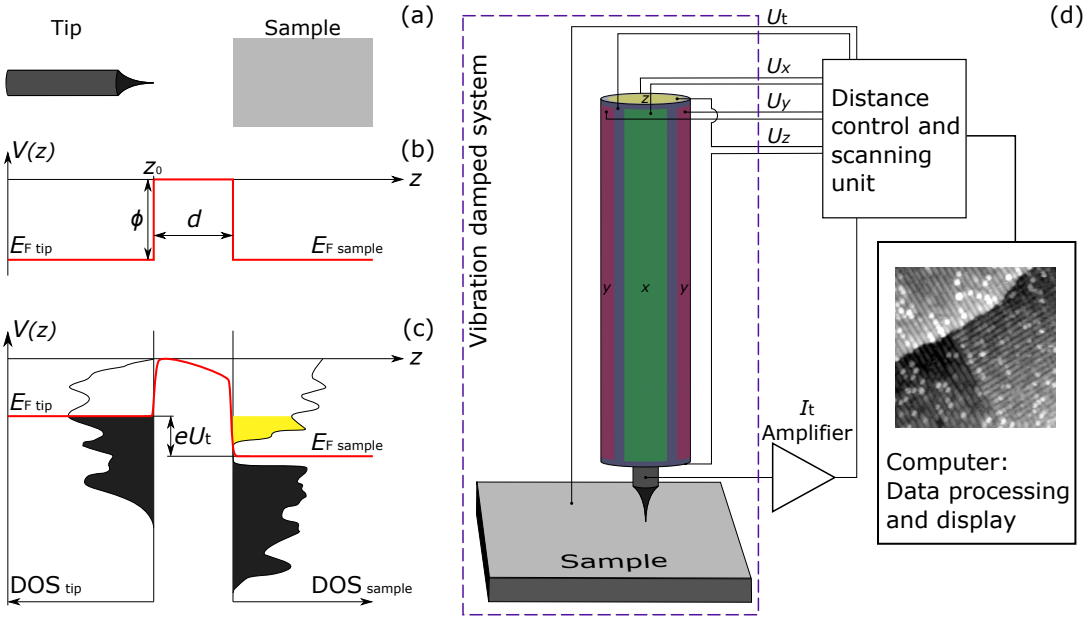

FIGURE 2.1: Schematic representation of an STM. (a) Arrangement of tip and sample with a gap in between, as used for STM. (b) Simplest one-dimensional model of the potential $V(z)$ for the configuration shown in (a). (c) An extended model for the configuration of a metallic tip and a positively biased (U_t) semiconductor sample. The densities of electronic states (DOS) and the tunnelling voltage are additionally taken into consideration. (d) Simplified schematic representation of an STM and its scanning mechanism.

$$\left(-\frac{\hbar^2}{2m}\frac{\mathrm{d}^2}{\mathrm{d}z^2}+V(z)\right)\Psi(z)=E\ \Psi(z), \qquad V(z)=\begin{cases}-\phi, & z<z_0\\ 0, & z_0<z<z_0+d\\ -\phi, & z>z_0+d\end{cases} \tag{2.1}$$

$$\Psi(z)\propto e^{-\kappa z}, \quad z_0<z<z_0+d, \quad \kappa=\sqrt{\frac{2m\phi}{\hbar^2}} \quad \Rightarrow \quad I_\mathrm{t}\propto\frac{|\Psi(z_0+d)|^2}{|\Psi(z_0)|^2}\propto e^{-2\kappa d} \tag{2.2}$$

2.2 X-ray photoelectron spectroscopy - XPS

XPS is used to determine the chemical composition of the sample surface within depths of about 10 nm; at the same time contamination can be detected.

A simplified model of XPS is illustrated in Figure 2.2(a). The sample is irradiated with X-ray photons of a specific given energy $E_{\text{photon}} = h\nu$, and electrons are produced through the photoelectric effect, leaving electron holes behind. The distribution of the photoelectrons as a function of their kinetic energy is measured by an analyser, which is usually biased by a variable retarding voltage U. Within this process energy has to be conserved, as stated in Equation 2.3 and illustrated in Figure 2.2(a).

$$E^{\text{photo}}_{\text{kin analyser}} = E_{\text{photon}} - E_{\text{binding}} - eU - \phi_{\text{analyser}} \tag{2.3}$$

It has to be pointed out that the kinetic energy of the photoelectrons measured at the detector does not depend on the work function of the sample ϕ_{sample} but is instead related to the work function of the analyser ϕ_{analyser}. Furthermore, only the photoelectrons, which have an energy high enough to reach the analyser ($E_{\text{kin analyser}} > 0$), are measured. In order to get the energy distribution function of the photoelectrons a hemispherical analyser can be used. This type of analyser has a built-in "notch filter", such that only electrons within a very small range in kinetic energy, depending on the retardation voltage U, are measured at the same time. By using Equation 2.3 the distribution in kinetic energy can be expressed as a function of the binding energy of the electrons; this is how XPS spectra are usually presented.

As already explained, core electron holes are produced by the the photoelectric effect using X-rays. These holes can, *inter alia*, decay by the emission of Auger electrons, which in turn contribute to the signal in the XPS measurement. As an example, the KLL-Auger process is explained here, as illustrated in Figure 2.2(b): Due to photoemission, there is an electron hole in the K-shell, which is filled up by an L_1-electron. The energy released by this process is used to liberate a so-called Auger electron from a higher shell (here $L_{2,3}$). Energy has to be conserved for this process, as stated in Equation 2.4, where E_K, E_{L_1} and $E_{L_{2,3}}$ are the binding energies of the electrons in the K, L_1 and $L_{2,3}$ shell, respectively.

$$E^{\text{Auger}}_{\text{kin analyser}} = E_K - E_{L_1} - E_{L_{2,3}} - eU - \phi_{\text{analyser}} \tag{2.4}$$

It has to be noted that the energy of an Auger electron does not depend on the photon energy, differently from photoelectrons. Furthermore, if the XPS spectrum is displayed as a function of the binding energy, the Auger peaks appear at "binding energies" according to Equation 2.3, which are not the actual binding energies of the electrons involved in that process.

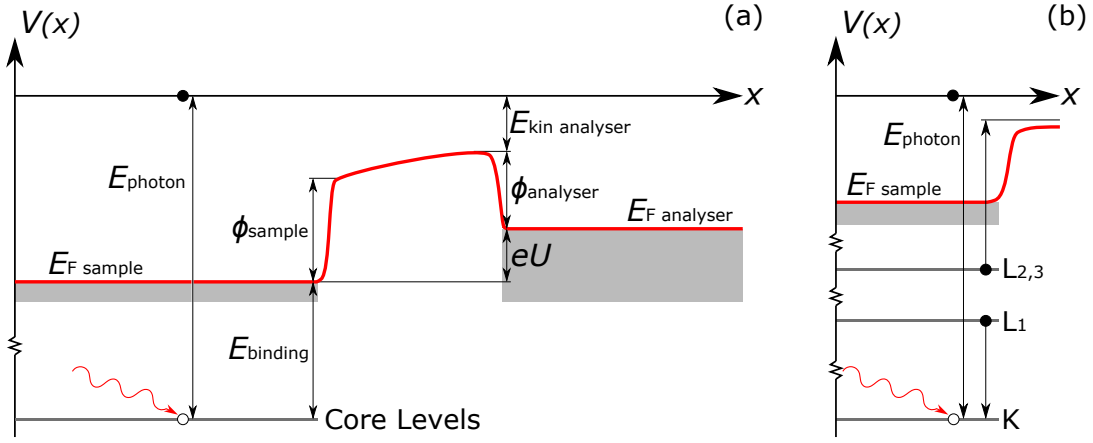

FIGURE 2.2: Schematic illustration of XPS. Note that the scales in both figures are distorted (marked by the zig-zaged line). (a) Photoemission process: Potential of a configuration consisting of a sample and an analyser, which is biased by a retarding voltage U. Electrons are liberated by X-ray excitation (photoelectric effect) and measured by an analyser. During this process energy has to be conserved according to labels in this figure and to Equation 2.3. (b) Auger electron process: An electron in the K-shell is filled by an L_1 electron, while an $L_{2,3}$ electron is released as an Auger electron.

For that reason, an XPS spectrum consists of photoelectron peaks as well as Auger electron peaks, which both correspond to specific elements in the sample. The information depth of a few nanometers arises from the inelastic mean free path of electrons, which is significantly smaller than the penetration depth of the X-rays.

2.3 Low-energy electron diffraction - LEED

LEED allows to get information about the degree of crystallinity of a sample and the periodicity of eventual surface reconstructions. A low-energy electron beam (energy $\sim$ 100 eV) hits the surface of the sample, usually perpendicularly, and the diffracted electrons are made visible on a phosphor screen, as shown in Figure 2.3(a).

According to kinematic scattering theory in far field approximation, the intensity of a scattered beam is the Fourier transform of the scattering potential. This means that a periodic potential caused by a periodic arrangement of atoms on the sample

surface results in regularly-arranged sharp spots in the diffraction pattern. The directions, in which the scattering is favoured, can be determined by the Ewald construction, which is illustrated in Figure 2.3(b). This construction is performed in the reciprocal space where the vector $\vec{k}$ is proportional to the velocity $\vec{v}$ of the electrons in the beam, as labelled in Figure 2.3(b) with m being the electron mass and h being the Planck's constant. Within this construction there are two constraints for possible vectors $\vec{k'}$ describing scattered electrons. (1) The first constraint is that only elastically scattered electrons are considered, since they contribute to the diffraction pattern the most. For that reason, inelastically scattered electrons and secondary electrons are filtered out on purpose, using a retarding field grid. This means that the energies of the electrons contributing to the LEED pattern remain unchanged throughout the scattering process and therefore the absolute value of $\vec{k}$, referring to the incoming beam, and the absolute value of $\vec{k'}$, describing the scattered beam, have to be equal. Each individual vector $\vec{k'}$, which underlies this constraint lies on the so called Ewald sphere. (2) The second constraint is referred to as Bragg's law, which takes into account the crystallinity of the sample and defines possible vectors $\vec{k'}$, for which constructive interference is occurring, meaning that electrons of a given energy are preferentially scattered into these directions. Bragg's law is presented in Figure 2.3(b), with the symbol $||$ meaning that only the component parallel to the sample surface is taken into account. In this formula, n represents an arbitrary integer and $\vec{G}$ is the surface reciprocal lattice vector, defined in Figure 2.3(b). In this context $\vec{d}$ is the corresponding lattice vector of the crystalline sample in real space. Due to the fact that during a LEED measurement only the near-surface region is probed, the scattering potential can be considered as purely two-dimensional, resulting in a corresponding reciprocal lattice consisting of equally-spaced, infinitely long rods, as illustrated in Figure 2.3(c). Therefore Bragg's law describing a two-dimensional scatterer is represented by these so-called reciprocal lattice rods, in case it is plotted in reciprocal space. Within this theoretical modelling of the observed LEED patterns, both of the constraints have to be fulfilled at the same time, meaning that the observed intensity maxima lie on the intersection points of the reciprocal lattice rods and the Ewald sphere.

In general, the following results can be obtained in LEED analyses. In case the probed surface is single crystalline the observed pattern gives information about the unit cell of the surface and possible reconstructions. If there are several different surface reconstructions coexisting at the same time the observed LEED pattern is

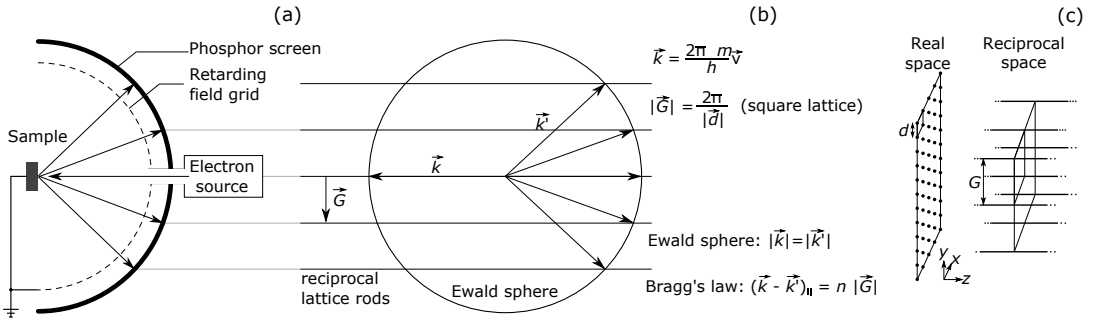

FIGURE 2.3: Schematic illustration and Ewald construction of LEED. (a) Experimental setup for a LEED measurement. (b) Ewald construction of the diffraction pattern of a LEED experiment. Possible scattering vectors $\vec{k}'$ start from the center of the Ewald sphere and end at the intersection points of the Ewald sphere and the reciprocal lattice rods. (c) Illustration of a two-dimensional lattice in real space and its corresponding reciprocal lattice consisting of rods in reciprocal space.

a superposition of the individual patterns. In case of a polycrystalline sample, the probed surface consists of a high number of individual crystals and therefore it is virtually impossible to identify single patterns, whereas noncrystalline samples lead to almost the same result, which is a uniformly illuminated screen.

2.4 Reflection high-energy electron diffraction - RHEED

RHEED is a technique to obtain information on the surface structure of crystalline samples, and to monitor growth processes. A beam of high-energy electrons (energy 10-100 keV) hits the sample under a grazing angle. The electrons are scattered by the surface atoms, and the diffracted electrons are detected on a phosphor screen, as shown in Figure 2.4(a). The deposition unit depicted in Figure 2.4(a) is not necessary for the RHEED process but rather shows a typical application in practice.

The modelling of RHEED is done in an analogue way as LEED, namely by kinematic scattering theory in far field approximation. This means that the intensity distribution on the screen is the Fourier transform of the scattering potential and therefore a periodic arrangement of atoms on the surface results in a corresponding periodic diffraction pattern. The directions, in which scattering is favoured in RHEED, can be determined by the Ewald construction, illustrated in Figure 2.4(b). Analogue to the Ewald construction of LEED, for a given beam energy, maxima in intensity are located at the intersection points of the Ewald sphere and the reciprocal lattice rods [representing Bragg's law, see Figure 2.3(b)]. These intersection points lie on

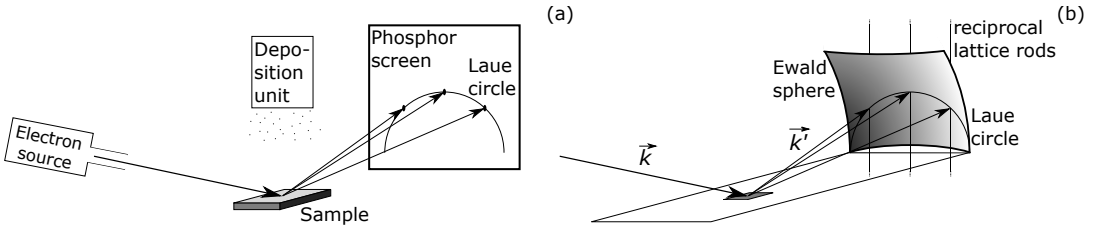

FIGURE 2.4: Schematic illustration and Ewald construction of RHEED. (a) Experimental setup for a RHEED measurement. (b) Ewald construction of the diffraction pattern of a RHEED experiment.

so-called Laue circles, as shown in Figure 2.4(a) and (b).

Compared to LEED, one significant advantage of RHEED is that it is possible to perform this technique while depositing a film onto the sample, as illustrated in Figure 2.4(a). This is possible because the incoming beam as well as the measured scattered beams confine grazing angles with the surface, and therefore there is enough space for a deposition unit, which has to be placed in front of the sample to ensure uniform growth. Within this application it is common to record the intensity of the specularly reflected beam as a function of time while depositing a film. The measured signal provides information about the growth mode, as shown for two prototypical examples in Figure 2.5: The Frank-van der Merwe growth and the Volmer-Weber growth.

The Frank-van der Merwe growth, also called layer-by-layer growth, is characterized by oscillations in the RHEED intensity of the specular reflected beam, as depicted in Figure 2.5(a). In this context, one oscillation represents the formation of a single layer, as illustrated in Figure 2.5(b) and described as followed. The starting point (1) and the other peaks in the intensity, *e.g.* point (4), are characterized by a flat surface without any islands or gaps. Deposition leads to the formation of single-layer-high islands and a resulting decrease in RHEED intensity, until a coverage of roughly 20-30 % is reached, corresponding with a minimum in the signal [point (2)]. As the deposition proceeds, the islands grow further, coalesce and the gaps in between them are filled up [point (3)], characterized by a raise in intensity, until the layer is completed, represented by (4). Due to the fact that this growth mode is so well defined it is possible to determine the thickness of a film simply by counting the number of oscillations during its growth, allowing for a real-time submonolayer control.

The Volmer-Weber growth is characterized by an exponential decrease in RHEED intensity due to formation of three-dimensional islands, as shown in Figure 2.5(c)

and (d). When the deposition process starts, islands are formed on the substrate, resulting in a decrease in the RHEED intensity, as shown by comparing point (1) and (2). However, these islands are more likely to grow in height rather than in the lateral direction, resulting in the formation of 3-dimensional islands and causing a further decrease in intensity [points (3) and (4)]. In practice, the intensity stays approximately constant at a certain point, which is reached when the gaps in between the islands are filled up, and therefore the islands grow the same amount in height as in the lateral direction.

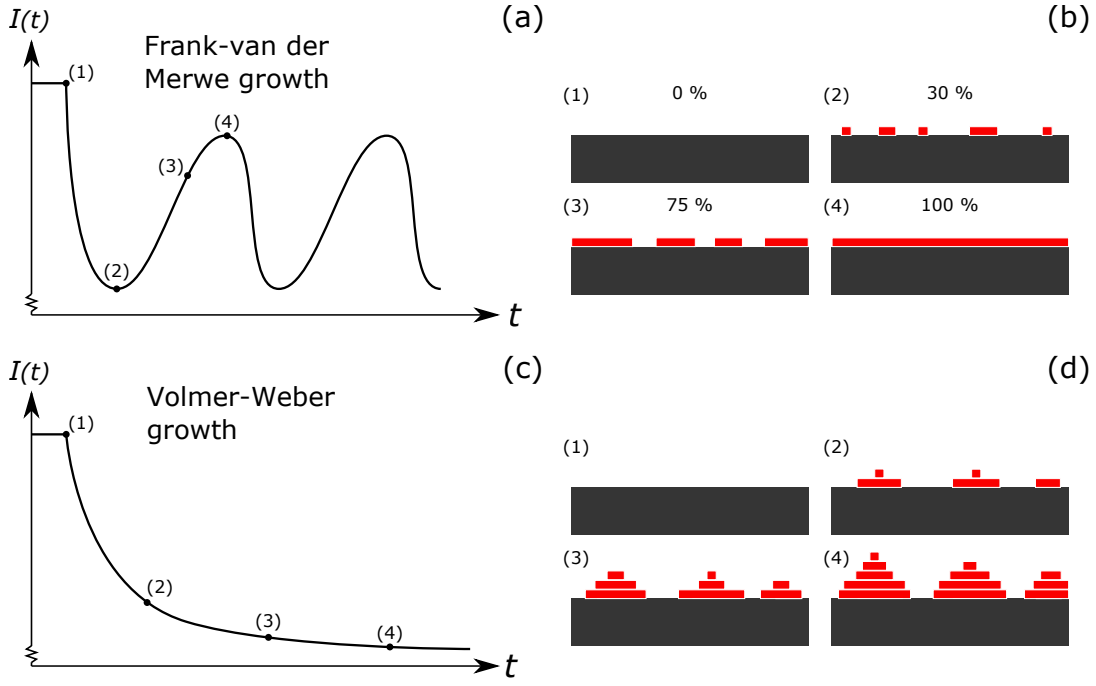

FIGURE 2.5: Growth modes measured by RHEED, monitoring the intensity of the specularly reflected beam. (a) RHEED intensity curve of a Frank-van der Merwe growth (layer-by-layer). (b) Schematic representation of the Frank-van der Merwe growth for given times, as labelled in (a). (c) RHEED intensity curve representing the Volmer-Weber growth (island growth). (d) Schematics of the Volmer-Weber growth for given times, as labelled in (c).

2.5 Molecular beam epitaxy - MBE

Molecular beam epitaxy is a technique to deposit thin films on substrates by a molecular beam, *e.g.* vapor, in high vacuum or ultra-high vacuum environment. The emphasis in MBE is to produce crystalline films, which is achieved by using well-prepared single-crystalline substrates and low deposition rates. If substrate and deposited material are chosen properly, it is possible that the film adopts the

crystalline structure of the substrate and grows accordingly. The most important parameters, which influence the structure and quality of MBE-grown films, are background gas and pressure, as well as substrate temperature and growth rate.

Depending on the material one wants to grow, and on which parameters one would like to have an influence on, numerous different realizations of MBE setups can be obtained. In the following the functionality of a low-temperature effusion cell is explained, which is schematically shown in Figure 2.6(a). Such a system was used to deposit strontium by means of MBE within the experiments described in this thesis. The low-temperature effusion cell is attached to the vacuum system via a CF flange, which provides feedthroughs for electrical power and cooling water. The evaporator itself has a shell structure: The inner shell (gray) is a crucible, which contains the material one wants to deposit. The second shell (red) is used for electrical heating and consists of heating filaments [not explicitly shown in Figure 2.6(a)]. Finally, the outer shell (blue) provides water cooling to guarantee that the heat is confined in the crucible. During operation the cooling water circuit is running and electric power is provided to heat the crucible to a specific temperature, typically in the range between room temperature and 800 °C. The heat causes the material inside the crucible to vaporize, and form a molecular beam that rises towards the substrate, as shown in Figure 2.6(a). The flux of the molecular beam and therefore the growth rate of the film on the substrate is mainly determined by the heating temperature. Typically, such systems are equipped with an instrument that can measure the deposition rate, *e.g.* a quartz crystal microbalance [not shown in Figure 2.6(a)]. In case the growth rate is known, it is rather simple to deposit well-defined amounts of material just by depositing material for an appropriate duration.

2.6 Pulsed laser deposition - PLD

Pulsed laser deposition is a technique to grow films where a pulsed laser is used to ablate material from a target in order to deposit it onto a properly aligned substrate. Also for this technique the aim is to grow films epitaxially, which means that the atoms in the film have a crystalline order corresponding to the one of the substrate. The properties of films grown by this process depend on numerous different parameters, with the background gas and its pressure, the substrate temperature and the fluence of the ablation laser being the most important ones. In this context, the fluence is a measure of the energy density of the laser beam, which has to be empha-

sized, since it not only determines the growth rate, but also the average energy of the particles being deposited, a parameter that cannot be varied in MBE experiments.

As an example, a schematics of our PLD chamber is shown in Figure 2.6(b) and explained here. A pulsed ultraviolet (UV) ablation laser with adjustable fluence is used to shoot on the target made of the material one wants to grow. Each single pulse has a high enough fluence to ablate material from the target. The ablated material forms a plasma plume, and it condenses on a well-aligned substrate. In order to control the sample temperature, the system is equipped with an infrared (IR) heating laser with adjustable power. An infrared pyrometer is used to monitor the temperature of the sample during the heating process. Furthermore, the system is equipped with a gas inlet allowing to choose the background gas and define its pressure. Finally, the PLD chamber is equipped with RHEED, allowing to live-monitor growth processes, to gather information about the growth mode, and to estimate the total amount of deposited material.

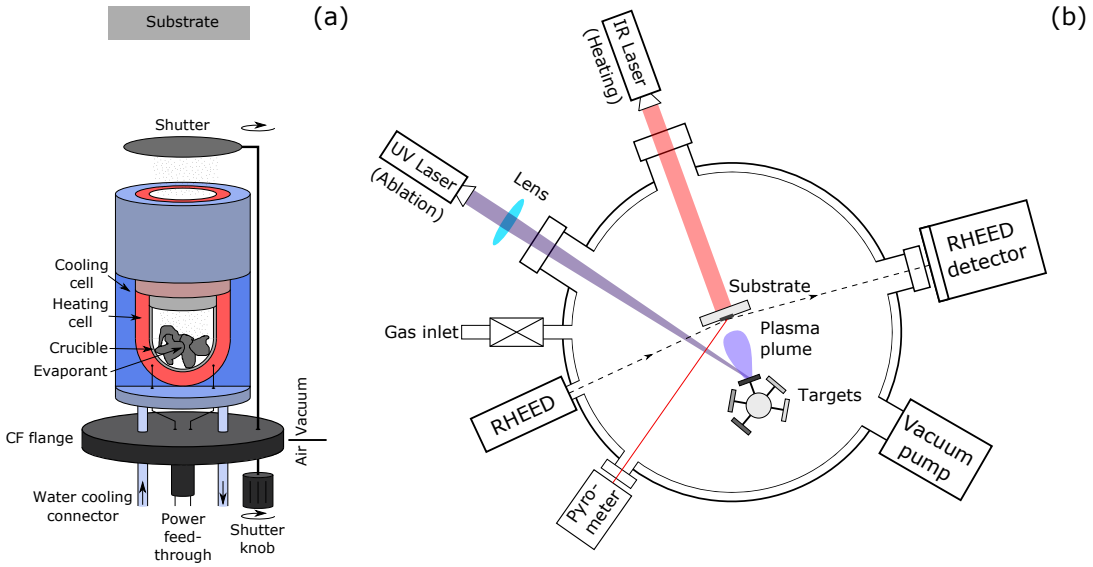

FIGURE 2.6: Schematics of an MBE and a PLD experimental setup, as they were used within the experiments described in this thesis. (a) Schematics of a low-temperature effusion cell used for MBE. Note that the cell is cut open in this representation in order to see its inside. (b) Illustration of the PLD process.

3 DESCRIPTION OF THE VACUUM SYSTEM

This section provides a detailed description of the vacuum system, in which essentially all of the experiments were performed. First, a general overview of the system and the standard equipment in terms of pumps and pressure gauges is presented. The following gives a detailed characterization of each individual chamber alongside with an exact description of how elementary operation steps such as, *e.g.*, sputtering or LEED were performed using the provided instrumentation.

3.1 Overview of the vacuum system

A complex system consisting of four vacuum chambers functioned as a workplace where essentially all of the experiments were performed. A schematics is depicted in Figure 3.1 with the round objects representing the four chambers (preparation, analysis, transfer, and PLD chamber), while the rectangular labels indicate the techniques and instrumentation provided by each of them. All four chambers are connected so that samples can be transferred using transfer sticks, without being exposed to atmosphere. Even though all of the chambers are connected, each of them is pumped down to ultra high vacuum (UHV) separately, and there are gate valves, indicated by the red double triangles in Figure 3.1, making sure that each chamber is a vacuum system on its own. This is an important fact, because in case there is a leak only one chamber will be affected. Furthermore, it is possible to run a single chamber on a different pressure, (*e.g.* during a deposition process), without having an effect on the rest of the system. Movements of samples inside the system can be performed by transfer sticks and manipulators, as schematically shown in Figure 3.2. Transfer sticks allow motions with two degrees of freedom, translation in one direction and rotation around its axis (polar rotation), and manipulators allow motions with five degrees of freedom: translation in all three spatial directions,

rotation of the whole manipulator around its axis (polar rotation) and rotation of the sample holder with respect to its axis (azimuth). In our system we use transfer sticks to transfers samples between the chambers and to put samples into the *in vacuo* storages. Manipulators are used to move samples inside a single chamber in order to position them, *e.g.*, in the center of the ion beam for a sputtering process.

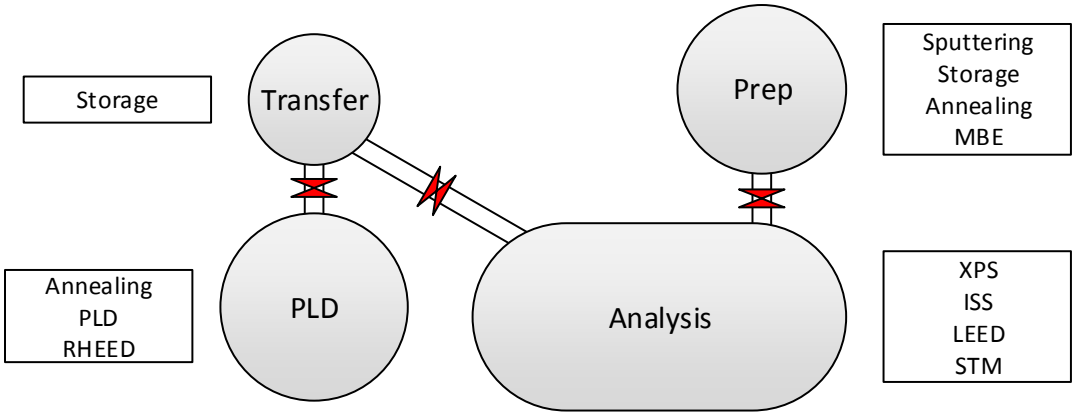

FIGURE 3.1: Schematics of the vacuum system. The round objects represent the four chambers. The rectangles represent the techniques provided in the chambers. The red double triangles indicate valves.

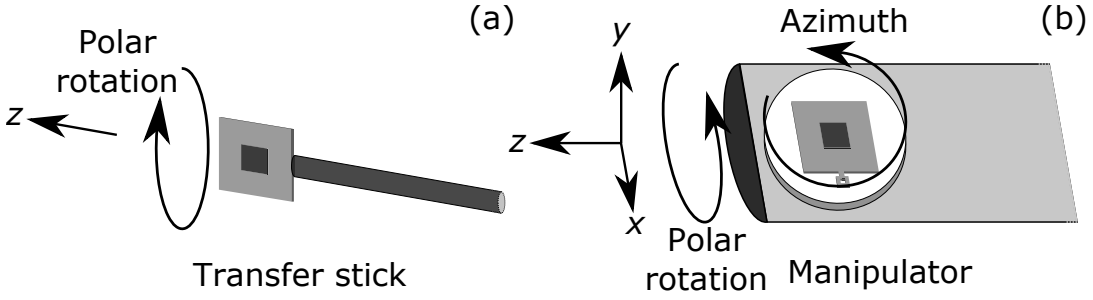

FIGURE 3.2: (a) Transfer stick. (b) Manipulator. The degrees of motion are labelled.

3.2 Pumping system

Each of the four chambers is provided with its own pumping system, which consists of a turbomolecular pump that is backed up by a scroll pump. Additionally, all of the chambers are equipped with an ion pump, which functions as a second independent pumping system. This particular setup is shown in Figure 3.3(a). Via gate valves one can switch between the two pumping systems. The base pressure of each individual chamber is below 10^{-10} mbar after bakeout.

Scroll pump

In our system we use oil-free Varian SH-110 scroll pumps [shown in Figure 3.3(b)] by the manufacturer Agilent Technologies as primary pumps to provide pressures of 10^{-2}-10^{-3} mbar at the exhaust of the turbo pumps. During operation two spiral-shaped parts are performing an eccentric motion without rotating with respect to each other, as depicted in Figure 3.3(c). At the beginning of each cycle air can flow inside a part of the spiral configuration indicated by the coloured part in Figure 3.3(c), while the movement of the spirals causes confinement of the part flooded with air and transfers it towards the center where the exhaust is located.

Turbomolecular pump

Turbomolecular pumps (turbo pumps) manufactured by Pfeiffer Vacuum GmbH are used to provide base pressures below 10^{-9} mbar for our experiments. In order to achieve such low pressures, pumps of this type have to be backed up by primary pumps, providing rough vacuum at the turbo pumps' exhausts. An image of a turbo pump is depicted in Figure 3.3(d), showing that the pump can be easily mounted to a vacuum system via a CF flange. Moreover, it shows the inner structure as well, consisting of rotors and stators, on which plates are mounted under specific angles, also schematically shown in Figure 3.3(e). While the pump is running, the rotors are spinning rapidly and gas molecules hitting the blades are deflected towards the exhaust. The pump performance depends on the rotation frequency and it is maximized if the rotation speed matches the average velocity of the gas molecules. In practice however, there are usually different gas species in the residual gas and not all of them are pumped with the same effectiveness. This typically causes a relatively high amount of hydrogen and helium in the residual gas, since the pumps are optimized for pumping heavier gas molecules. Due to their operation principle turbo pumps are also well suited for pumping noble gases.

Ion pump

For the third type of pumps, we use Varian VacIon StarCell ion pumps manufactured by Agilent Technologies. Ion pumps are based on the principle of binding and capturing gas rather than transferring it away from the system, in contrast to the previously-discussed types of pumps. Figure 3.3(f) depicts the exact type of ion pump used in our system, while the inner structure of such a pump is schematically shown in Figure 3.3(g). It contains two cathodes consisting of titanium and a grid of hollowed cylindrical anodes (only two are shown in this simplified representation) in between, biased by a voltage typically in the range of 1-10 kV. Furthermore,

there are magnets providing a magnetic field parallel to the cylinders. The pumping mechanism works as described in the following. Free electrons in the pump are accelerated towards the anode. However, due to the magnetic field and the corresponding Lorentz force, they are forced on spiral tracks resulting in a magnetron motion inside the cylindrical anodes, as indicated in Figure 3.3(g). If such an electron hits a gas atom, it can ionize it by collision. As a result of this process one or more additional electrons are released, which maintain the ionization mechanism within this pump. The positively charged ion, on the other hand, is accelerated towards the titanium cathode and impinges with a high kinetic energy. This causes the cation to penetrate deep inside and be buried there. At the same time, Ti from the cathode is sputtered away, and adsorbs at the anode, the cathode and the inside walls of the pump, forming a highly reactive surface, which chemically binds gas molecules and also contributes to reducing the residual pressure. Since noble gases are inert they are not pumped well by an ion pump.

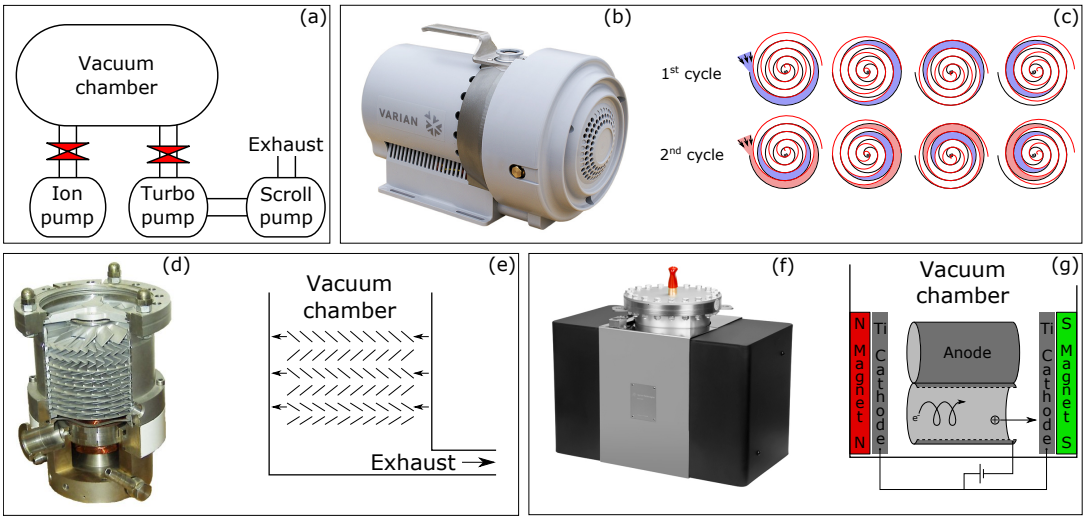

FIGURE 3.3: Schematics of different vacuum pumps. (a) Pumping setup of each of our vacuum chambers. (b) Picture of a Varian SH-110 scroll pump, reprinted from [17]. (c) Illustration of the working mechanism a scroll pump. (d) Photograph of a turbomolecular pump, reprinted from [18]. (e) Schematics of a turbomolecular pump. (f) Photograph of a Varian VacIon 300 StarCell Ion Pump, reprinted from [19]. (g) Schematics of the structure and functionality of an ion pump.

3.3 Pressure measurement

In order to measure the pressure inside the vacuum system, each individual chamber is equipped with a Bayard-Alpert pressure gauge. Due to the fact that they cover

a wide measurement range in the high vacuum and ultra-high vacuum regime, they are wide spread in such applications. The PLD chamber however is capable of providing higher pressures compared to the other chambers. Therefore, it is equipped with a capacitive pressure gauge as well as with a Pirani gauge allowing to measure higher pressures. The composition of the residual gas on the system can be determined by quadrupole mass spectrometers, which are present in the preparation, analysis and PLD chambers. Such analysers are also a useful tool to detect gaseous contaminations and to perform leak checks.

Bayard-Alpert pressure gauge

Bayard-Alpert cells are quite commonly used as pressure gauges in vacuum systems due to their wide operating range extending from 10^{-3} to 10^{-10} mbar. The pressure measurement within such gauges is indirect because electrical quantities are measured, which are proportional to the density of gas molecules and in turn to pressure, as explained below.

A schematic representation of a Bayard-Alpert cell is depicted in Figure 3.4(a). As indicated, the cell is typically mounted on a CF flange, which makes application to a vacuum system rather simple. The gauge consists of a heated-filament electron source, a helical winded anode, and a thin rod in its center, referred to as ion collector, which functions as a cathode. The electrons that are released at the source are accelerated towards the anode, pass the windings, and ionize gas molecules in its enclosed volume. The positively charged ions are then attracted by the ion collector, which is supplied with a voltage lower compared to the potential of the electron source. When the ionized residual gas molecules hit the ion collector, an electrical current is generated, and then amplified and measured. This current depends on the density of gas molecules in the system, which in turn is proportional to the pressure. Note that the current also depends on the ionization probability, which differs for different gas species. To explain this effect, let us consider two systems, which are under the same real pressure. The first one is filled with N_2, while the second one is filled with CO_2, which has a higher ionization probability compared to N_2. Therefore, a higher ion current is measured and a higher pressure is displayed by a Bayard-Alpert pressure gauge in the second system. In case the residual gas in the vacuum system is known, one can more accurately estimate the real pressure by dividing the displayed pressures by relative ionization probabilities. These probabilities are empirically determined and lie in a range between 0.16 (He) and 10 (high-order carbon hydroxides), while being normalized to 1.0 (N_2).

For pressures exceeding 10^{-2} mbar the measured current is produced by a glow discharge, a physical phenomenon that is independent on the pressure. Therefore, this pressure defines the upper end of the measuring range.

Capacitive pressure gauge

Capacitive pressure gauges designed for vacuum applications typically have a range of 10^{-3} mbar to ambient pressure. Our specific gauge was characterized by a $10^{-3} - 1$ mbar range. Thus, in combination with a Bayard-Alpert gauge, they allow to extend the measurement range. The pressure measurement within capacitive gauges is direct and independent on the composition of the residual gas in the system.

As shown in Figure 3.4(b), the inside of the capacitive gauge is separated into two parts by an elastic membrane. One part is connected to the vacuum chamber while the second part is under a well-defined reference pressure, resulting in a deformation of the membrane, which depends on the pressure. Within such applications the membrane is coated with a metallic film, which allows to quantify its deformation, and in turn the pressure by measuring the capacitance between the metal coating and a second electrode, as depicted in Figure 3.4(b).

Pirani gauge

Pirani gauges cover a measurement range from 10^{-4} mbar to near-ambient conditions and can thus be used as an alternative to capacitive gauges, but also as an independent addition due to their different functioning principle.

The functionality is based on the phenomenon that a heated wire looses heat by transferring thermal energy to the gas atoms and molecules hitting it. Within the gauge a constant electric current is passed through a filament causing its temperature to reach an equilibrium defined by the rate of the gas molecules hitting it, which in turn is directly proportional to the pressure. Exploiting the relation between electrical resistance and temperature, the determination of the filament temperature is reduced to a measurement of its resistance, using a bridge circuit for example.

Quadrupole mass spectrometer

Quadrupole mass spectrometers are used to determine the partial pressures of the residual gas composition, and to perform leak checks. Within this process the residual helium pressure in the system is measured while applying pulses of He on the parts to be checked from outside. In case there is a leak a significant increase in the He signal is recorded.

As schematically shown in Figure 3.4(c), this type of analyser consists of four parallel metal rods. A source provides a voltage consisting of a DC part superimposed with an AC part between neighbouring rods, while opposing rods lie on the same potential. Via these rods a time-dependent electrical quadrupole field is generated. Residual gas molecules are ionized [not explicitly shown in Figure 3.4(c)] and then enter the quadrupole mass spectrometer via an entrance hole. From there on the ions take rather complicated trajectories, whereby for a given ratio of the applied voltages only ions within a specific interval in mass-to-charge-ratio can pass the rods and hit the detector, as indicated by the blue curve. The trajectories of ions outside this interval are extremely unstable and result in the ions hitting the rods instead of the detector, as shown by the red curve. During a measurement the ratio of the applied voltages is scanned and therefore the mass-to-charge ratio of ions, which can pass the quadrupole field is scanned, while the number of hits at the detector is measured. This provides a spectrum as a function of the mass-to-charge ratio, from which the relative amounts of specific gas species in the residual gas can be estimated. Interpretation of such spectra has to be done quite carefully since peaks at certain mass-to-charge-ratios generally do not correspond to specific ions in a unique way, as for example N_2^+ and CO^+ both have a mass-to-charge-ratio of 28.

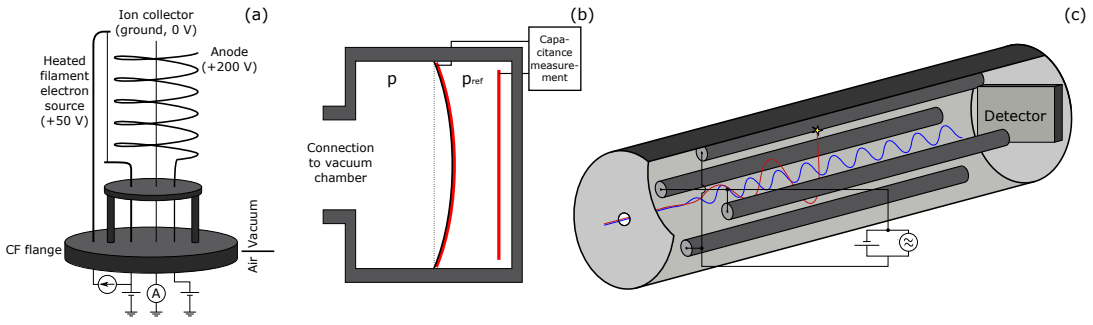

FIGURE 3.4: (a) Bayard-Alpert pressure gauge. (b) Capacitive pressure gauge. (c) Quadrupole mass spectrometer.

3.4 Preparation chamber

As shown in Figure 3.1, the preparation chamber is mainly used to prepare samples by sputtering, annealing, or molecular beam epitaxy. A manipulator is used to position the sample for the respective processes, and in order to perform them in a reproducible way, always the same parameters were used, which are presented in the following. The preparation chamber also provides a storage unit, which can contain

up to seven samples, and a loadlock connected to it is used to insert samples into the system.

Sputtering

Sputtering is a technique used to clean sample surfaces by bombarding them with noble gas ions. Within this process the first couple of atomic layers together with eventual surface contaminations are removed. Since this process also causes a rearrangement of the atoms, introduces defects, and roughens the surface, annealing has to be performed afterwards to heal these defects.

In order to perform sputtering, argon is let into the chamber until a pressure of 3.0×10^{-6} mbar is reached. The Ar atoms are ionized and accelerated by an electric field such that they hit the sample with a kinetic energy of 1 keV, resulting in sputter currents of approximately 5-10 µA. Within this thesis we performed cycles of sputtering lasting 10 min each.

Annealing in the preparation chamber

Annealing in the preparation chamber is performed by an electron beam produced by a hot filament. Since we use sample plates with a hole, the electrons directly impinge on the backside of the sample, which leads to a rather uniform temperature distribution. The sample temperature is measured by an infrared pyrometer and regulated by a control unit by adjusting the filament current. The annealing processes in the preparation chamber are characterized by the following parameters, unless otherwise noted. Oxygen is let into the chamber via a leak valve until a pressure in the range of $3\text{-}7\times10^{-6}$ mbar is reached. The sample is biased by +1000 V and then its temperature is ramped up at a specific rate, between 10 °C/min and 100 °C/min, until a temperature of 1000 °C is reached. The sample dwells at this temperature for 60 min in case of annealings after sputtering and for 30 min in case Sr or Ti has been deposited. Finally, the temperature is ramped down at the same rate used previously. The ramp rate we choose for a specific sample depends on the number of annealings it has already undergone. For the first annealing of a sample a ramp rate of 10 °C/min is used, which is progressively increased in steps of 10 °C/min for each additional annealing, with the maximum ramp rate being 100 °C/min. There is a possibility that a sample cracks during an annealing process due to thermal stress and such an event is especially likely to happen during the first couple of annealings. By using a low ramp rate first, which is then progressively increased, this risk is significantly reduced.

MBE - Sr depositions

The MBE setup in the preparation chamber consists of a low-temperature effusion cell and an electron beam evaporator, used to deposit strontium and titanium, respectively. All of the strontium depositions carried out within this thesis were performed in the preparation chamber using the Sr-evaporator, schematically shown in Figure 2.6(a), and explained in Section 2.5. In preparation for Sr depositions, the evaporator is heated to 480 °C for 20 min, followed by 40 min at 420 °C in order to outgas the system, and to let the evaporation rate stabilize. After that, the temperature is still kept at 420 °C for the deposition process. In regular intervals (typically once in two weeks) the deposition rate is measured and calibrated, using a quartz crystal microbalance (QCM). This device allows to determine the amount of material deposited onto a piezo-crystal, by measuring the change in its resonance frequency. The method is quite accurate since it can detect changes in the sub-monolayer range. Once the deposition rate is known, the actual deposition can be performed, which consists of aligning the sample while having the shutter closed and then opening it for a specific period of time corresponding to the amount of material one would like to deposit. In this particular setup the deposition rate was typically between 120 and 230 s/Å. After the deposition process is finished, always a 30 min annealing process is performed in either the preparation or PLD chamber.

The Ti-evaporator in this setup was defective at the beginning of this thesis and therefore, as an alternative, Ti depositions were performed by means of PLD in the PLD chamber (see Section 3.7). After the Ti-evaporator had been repaired, we opted not to use it in order to have the samples prepared the same way all the time, and, therefore, exclude any possible effects caused by a different sample preparation.

3.5 Analysis chamber

As illustrated in Figure 3.1, the analysis chamber is equipped with a variety of devices to perform surface characterization - comprising an X-ray source for XPS, a mass-filtered ion beam with raster unit for ion scattering spectroscopy (ISS), a hemispherical analyser, and an STM. A manipulator is used to move samples in this chamber and to align it for the different techniques.

XPS

For XPS analyses, an X-ray source manufactured by Scienta Omicron GmbH is used, which can supply aluminum K_α and magnesium K_α radiation. A hemispher-

ical analyser is used to determine the energy distribution of the photo- and Auger electrons generated in the process of irradiating the sample with X-rays. The XPS studies presented in this thesis are characterized by using aluminum K_α photons, which have an energy of E(Al-K_α)=1486.6 eV. The detector in our particular setup measures the distribution of kinetic energy of the electrons leaving the sample in perpendicular direction; the pass energy of the detector is set to 50 eV for survey spectra, and 10 eV for detailed core level spectra. Via Equation 2.3 the spectrum is expressed as a function of the the binding energy of the electrons. The wide-energy-range surveys presented in the experimental part of this thesis extend from binding energies between 1286 eV and -10 eV with a step size of 0.5 eV, whereas a step size of 0.05 eV is used for the detailed spectra of single peaks.

ISS

The analysis chamber also contains a mass-filtered ion beam with raster unit used for ion scattering spectroscopy (ISS). This technique is used to analyse the first atomic layers of samples, to gather information about the chemical composition of the surface, and to detect possible contaminants. During a measurement a helium-ion beam hits the sample surface and the distribution of the kinetic energy of He ions scattered in a specific direction is measured by the hemispherical analyser. Within the presented experiments no ISS analyses have been performed, and therefore this technique is just presented here to give a complete description of the vacuum system and its capabilities.

LEED

LEED measurements presented within this theses are characterized by a beam energy of 90 eV and a screen voltage of 6 keV. The electron signal is increased by a micro-channel plate and the patterns on the phosphor screen are photographed using a camera mounted to the system. This setup ensures that the images are taken in a reproducible way, which makes it easier to compare them. During one LEED measurement three different images are taken: The first one shows the pattern produced by the electron beam hitting the center of a crystalline sample. The second one is called dark field image, and it is taken on the same position on the sample but while the screen voltage is turned off. The third image, the so-called polycrystalline, is taken after moving the sample out of the beam, so that the pattern of the polycrystalline sample plate is photographed. These three images are used to remove spurious background contributions by recombining them to one final image by graphical data post-processing using the software ImageJ.

STM

The analysis chamber provides a SPECS Aarhus 150 variable temperature STM. For this type of STM, a tungsten tip is used, which has been produced by electrochemically etching a wire with KOH. A vibration-damping system decouples the STM block from the rest of the vacuum system, allowing to perform STM analyses, while, *e.g.*, having the pumps running or operating in a different chamber of the system at the same time. STM images presented within this thesis were taken at room temperature, and the samples were positively biased by a voltage in the range of 1.5-2.3 V with respect to the tip, meaning that empty states of the sample were probed. Tunnelling currents were typically in a range of 0.03-0.50 nA.

3.6 Transfer chamber

The transfer chamber is the smallest one of the system. It is used to transfer samples between the PLD and the analysis chamber. It also provides a storage for up to 20 samples.

3.7 PLD chamber

The main purpose of this chamber is to provide a sophisticated, software-supported setup to perform growth experiments by means of PLD, a technique explained in a general context in Section 2.6. Furthermore, this chamber is used to perform laser annealings during samples preparation. A detailed schematic of the PLD chamber is depicted in Figure 2.6(b). A loadlock connected to the chamber [not shown in Figure 2.6(b)] is used to insert the targets inside the system without breaking vacuum.

Annealing in the PLD chamber

Annealings are performed using an infrared (IR) heating laser manufactured by DILAS. This laser provides a beam of a wavelength of 980 nm, as well as a pilot beam in the visible range. The glass fiber directing both beams to the chamber is fixed, so that there is no possibility in moving the beam or changing its direction. We took advantage of this fact by using the beam of the pilot laser as a reference element to align samples reproducibly in a two-step process. First, the sample is roughly aligned by moving it to a home position according to the rulers on the manipulator.

This position however is not exactly reproducible because the specific manipulator used in this chamber is not very rigid, as it can slightly bend, for example, when putting samples into its pocket. In a second step, the sample is fine-aligned by adjusting its position such that it is centred with respect to the fixed beam.

During annealings, the sample temperature is monitored by an infrared pyrometer and regulated via software by adjusting the power of the heating laser. The annealings performed in the PLD chamber are characterized by the same set of parameters compared to those performed in the preparation chamber. The oxygen pressure is set to a value within the range of 3-7$\times 10^{-6}$ mbar and the temperature of the sample is ramped up at a rate between 10 °C/min and 100 °C/min until a temperature of 1000 °C is reached. The exact ramp rate for a given sample depends on how many annealings it has already undergone, as explained in Section 3.4. Then the sample temperature is kept at 1000 °C for 60 min in case of annealings after sputtering and for 30 min in case Sr or Ti has been deposited before, before being ramped down to room temperature at the same rate.

PLD - Ti depositions and growths of $SrTiO_3$

In order to perform PLD experiments the chamber is equipped with a pulsed ultraviolet (UV) laser manufactured by Coherent Inc. It provides laser pulses of a wavelength of 248 nm and a duration of 20-50 ns, and the fluence is adjustable by an attenuator. The laser beam is directed inside the chamber via an imaging system and focused to a rectangularly shaped spot of dimensions of 0.7$\times$1.7 mm^2 on the target. Up to five different targets can be mounted on a carousel, but only three of them have been used within this theses: TiO_2, 0.5 wt.% Nb-doped $SrTiO_3$(110), and undoped $SrTiO_3$(110). Two types of PLD growths have been performed, with the first one being represented by submonolayer Ti depositions at room temperature on $SrTiO_3$(110) samples as a preparation step. The second type represents the main experiments performed within this thesis and comprise various growth experiments of $SrTiO_3$ performed under different parameters. A RHEED from Staib Instruments GmbH is used to monitor these growths by measuring the RHEED intensity of the specularly diffracted beam.

The preparations for depositions are performed while having the sample not present in the PLD chamber and consist of target alignment, setting the laser fluence and preablation. The purpose of the preablation is to remove target material in the first few hundreds of nanometers, and thus get rid of possible contamination. Consequently, samples must not be in the PLD chamber during this process in order to

exclude any possibilities of depositing material onto them before the actual growth experiments. First, the targets are moved to a home position, which is saved on the software and defined by a certain configuration with respect to the fixed pilot beam of the IR laser. From there on, a certain target on the carousel is chosen and a rectangularly shaped scanning area is defined, by setting its height, width, and its offset coordinates with respect to the home position. Oxygen is let into the chamber to a pressure of 5×10^{-6} mbar and the fluence is set such that the preablation is performed under the same parameters that are used for the deposition. In order to set the fluence, the targets are temporarily moved down so that the beam can go straight through the chamber. A detector, placed behind the exit window of the chamber, is used to measure the total energy of single laser pulses. The fluence of the pulses hitting the target can then be calculated by dividing the measured energy by the spot size of the beam on the target and the transmission of the exit window. Finally, the position of the attenuator is adjusted via software such that the measured power corresponds to the desired fluence. Then, the selected scanning area is preablated by shooting with the laser while the target is being moved by software, such that each individual spot within the scanning area is shot 10-20 times.

Finally, the sample is transferred to the PLD chamber and aligned by the same two-step procedure used for annealings (explained above), resulting in a configuration of the sample being in the center of the IR laser beam, and sample and target being parallel with respect to each other, with a distance of 5.5 cm in between. Oxygen is let into the chamber to reach a pressure in the range of 3-7×10^{-6} mbar, a value, which was always used for the depositions within this thesis. From this point on, the further procedure differs between the two types of growths we performed: Submonolayer Ti depositions at room temperature and growth experiments of $SrTiO_3$.

For the Ti depositions at room temperature, the heating laser is not used and therefore one can directly proceed to re-setting of the laser fluence. This step has to be performed since its value can slightly change in the period after it has already been set in the preablation process. For Ti depositions always the same fluence is used, which is 2.5 J/cm^2 on the spot at the target, corresponding to an energy of 27.7 mJ/pulse (measured outside). Within this calculation, the spot size on the target (0.7×1.7 mm^2) as well as the transmission of the exit window is taken into account. Finally, Ti is deposited by shooting 1-5 laser pulses onto the preablated area of the TiO_2 target, depending on the amount of titanium that has to be deposited. The process is finished by annealing the sample for 30 min in either the

PLD or preparation chamber.

For the growth experiments of $SrTiO_3$, there is one additional step in the sample alignment, which consists of setting its azimuth and polar angles in order to have it aligned for RHEED. Upon rotations along the azimuth angle, the center of the sample stays at the same position and therefore the sample stays centred with respect to the beam of the IR laser. Before growth, the RHEED pattern (35 keV) of the pristine sample is photographed by a camera, mounted to the system, similarly as to the LEED setup. As a next step, the IR heating laser is turned on, ramping the sample temperature up to a value of 750 °C. The angular position in both azimuth and polar directions are then fine adjusted to optimize the RHEED pattern such that the specular spot can be followed throughout the deposition process. As a last preparation step, the fluence of the UV laser is re-set to the desired value and the tracking mode on the RHEED software is used to monitor the RHEED intensity of the specularly diffracted beam during the deposition. Finally, the growth process can take place by shooting laser pulses with a repetition rate of 1 Hz on the $SrTiO_3$ target (0.5 wt.% Nb-doped $SrTiO_3$ or undoped $SrTiO_3$) while it is being scanned according to the previously set and preablated scanning area. After the growth process is finished, the sample is still kept at 750 °C for additional 10 min before its temperature is ramped down to room temperature. Finally, the angular position of the sample is again fine adjusted such that a nice RHEED pattern of the film can be acquired.

4 RESULTS AND DISCUSSION

4.1 *Ex-situ* sample preparation and mounting

The STO(110) crystals, which were used as substrates within the experiments performed during this project, were bought from CrysTec GmbH Kristalltechnologie, Germany. In particular, they were 0.5 wt.% Nb-doped, with a size of $5\times5\times0.5$ mm^3, an angular miscut of $<0.3°$, and a polished surface. This miscut allowed to observe terraces on the surface, even in the STM images of size of 150×150 nm^2.

In prior experiments it turned out that the surfaces of the samples were contaminated with residues of calcium, an element that can be easily dissolved in water. In order to not only remove this type of contamination but also to get rid of possible residues from the mechanical polishing, an appropriate *ex-situ* cleaning was performed. This specific procedure consisted of cycles of sonication in Extran (neutral detergent, 3 % diluted in ultrapure water) and deionized (DI) water as well as boiling in water. In particular, each individual sample was sonicated in heated Extran for 20 min, rinsed in DI water, and sonicated in DI water for 10 min, and the whole process was repeated in a second cycle. Subsequently, each sample was boiled in DI water for 10 min. In order to avoid contaminating the sample with any organic substances, the flasks used for the cleaning procedure had been boiled in nitric acid and rinsed thoroughly in DI water before.

Each sample was then mounted on a plate through properly shaped clips, as shown in Figure 4.1(a), where both sample plate and clips consist of Nicrofer®, a high-temperature and oxidation resistant alloy mainly consisting of nickel, chromium, and iron. It has to be emphasized that such a sample mounting avoids any glues, which could degas upon annealing processes. By having a closer look at Figure 4.1(a), one can see that the clips consist of two steps spot welded to the plate. Furthermore, there is a spacer in its center, which is applying strain to the sample to keep it in position. The special design of the clips is necessary to keep the samples tight even

after several annealing cycles in order to be able to perform STM. The clips were fabricated by us by cutting stripes out of a foil, spot welding spacers onto it, and shaping them through a mould. The sample plates on the other hand were produced by a company, and as shown in Figure 4.1(b) and (c) they exhibit one important detail: There is a hole in its pocket, so that samples can be heated directly from their back side, leading to a rather uniform temperature distribution and causing samples less likely to crack during annealing processes. In order to avoid possible contamination of the sample during the mounting process, only clean clips and plates that had been boiled in nitric acid and rinsed in DI water before were used.

After mounting the samples, it was made sure that they were tight before inserting them to the vacuum system via the loadlock of the preparation chamber.

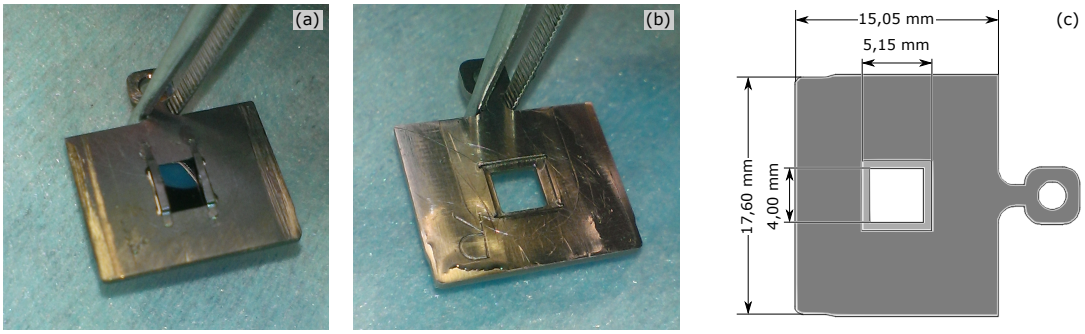

FIGURE 4.1: (a) Photo of a sample mounted on a plate through clips. (b) Photo of a plate without a sample on it, revealing a hole in the pocket. (c) Exact drawing of a sample plate with dimensions.

4.2 *In-situ* sample preparation

The *in-situ* STO(110) sample preparation consisted of sputtering and annealing cycles as well as depositions of strontium and titanium, respectively. The goal was to remove surface contaminations first, and then prepare a flat and well-ordered surface that is terminated by the (4×1) and (5×1) reconstructions coexisting at the same time. Among all the different surface reconstructions of STO(110) [see Figure 1.2] these two can be imaged especially well in STM, and it is also rather easy to distinguish them in high magnification images. Within the sample preparation, LEED images were taken to probe the surface reconstructions in order to estimate the amounts of Sr or Ti that have to be deposited to tune the surface towards the desired reconstructions. As a final step, STM was performed to image the prepared

(4×1)-(5×1)-reconstructed surface to check whether it was clean and well ordered enough to proceed with our experiments. The precise procedure of our sample preparation is illustrated by the flow chart shown in Figure 4.2, and as an example the sequence of steps of one typical sample is described in the following.

Once a new sample is inserted to the vacuum system, it is first test annealed in order to remove possible organic surface contamination by pyrolysis and to make sure it does not crack. This process is characterized by a duration of 2 hours, a temperature of 1000 °C, and an oxygen pressure of 3-7×10^{-6} mbar. For test annealings always a ramp rate of 10 °C/min is used to heat the sample and there are interrupts at 700 °C and 850 °C, respectively, to check whether the temperature distribution on the sample surface is sufficiently uniform to proceed. These precautionary measures are taken to limit thermal stress in samples and therefore to avoid samples to be cracked. However, it can eventually happen that a sample cracks during the preparation, which means that it cannot be used for further experiments and has to be discarded. Once a sample survives the test annealing, it is significantly less likely to crack in further annealings and therefore the intermediate stops are skipped and higher ramp rates are used.

As a next step, the sample is sputtered for 10 min using 1000 eV Ar ions and typical ion current of 5-10 µA, while there is a pressure of 3.0×10^{-6} mbar inside the chamber. After each sputtering cycle the sample is annealed for 1 hour at a temperature of 1000 °C in 3-7×10^{-6} mbar oxygen environment. Based on experience one cycle is not sufficient to render the surface of a new sample reasonably clean, and therefore this process is repeated twice such that each new sample undergoes in total three rounds of sputter-annealing.

At this point a LEED image is acquired using 90 eV electrons to probe the surface reconstructions. Based on this image a decision on the further preparation of the sample is made while the surface phase diagram of STO(110) [see Figure 1.2] is used as a reference. In general, the LEED analysis can have three different outcomes (explained below) but for new samples that have just undergone three cycles of sputtering and annealing the surface is typically determined by (6×4) and (2×4) reconstructions coexisting at the same time, as represented by the LEED image in Figure 4.3(a). According to Figure 1.2, this means that a certain amount of Sr has to be deposited to tune the current surface to the desired (4×1)-(5×1)-reconstructed one. The amount of Sr that has to be deposited is estimated by having a close look on the LEED pattern, *i.e.*, by comparing the relative intensities of the two patterns

corresponding to the (6×4) and (2×4) reconstructions, respectively.

Based on the LEED result, a certain submonolayer amount of Sr is deposited by MBE, characterized by low deposition rates, typically in the range between 120 and 230 s/Å, vacuum environment, and the substrate being at room temperature. As soon as the deposition is finished, the sample is annealed for 30 min at a temperature of 1000 °C in 3-7×10^{-6} mbar oxygen environment so that the atoms can rearrange according to the energetically most favoured structure to form surface reconstructions.

As shown in Figure 4.2, after the first deposition of Sr one has to go back one step and perform a further LEED analysis to check whether the right amount of Sr has been deposited to end up with the desired (4×1)-(5×1)-reconstructed surface. This time there are three possible outcomes: (1) The first possible and favoured LEED result represents a sample surface terminated by the (4×1) and (5×1) reconstructions coexisting at the same time, as shown in Figure 4.3(d). This is exactly the type of surface we use as a starting point for our further experiments. (2) The second possibility is obtained when too little Sr has been deposited and corresponds to a (4×1), (2×4) or (6×4) periodicity in the LEED pattern [see Figure 1.2]. For example, Figure 4.3(b) depicts a LEED image of a surface determined by the (4×1) and (2×4) reconstructions coexisting at the same time. In this particular case a further Sr deposition followed by annealing has to be performed in order to tune the surface to the desired direction. (3) The third possible outcome is obtained when too much strontium has been deposited, resulting in (6×1) or (5×1) patterns observed in LEED, as shown in Figure 4.3(c) for example. According to the surface phase diagram of STO(110) in Figure 1.2, a submonolayer amount of Ti has to be deposited in order to tune the surface to be (4×1)-(5×1) reconstructed. Such a process is performed by means of PLD in our setup. Depending on the amount one wants to grow, the deposition consists of shooting 1-5 laser pulses (wavelength 248 nm, duration 20-50 ns per pulse, fluence 2.5 J/cm^2) onto a TiO_2 target. The whole process takes place in oxygen environment under a pressure in the range of 3-7×10^{-6} mbar, while the substrate is kept at room temperature. A more precise description of the procedure of Ti depositions can be found in Section 3.7. Finally, the sample is annealed for 30 min under the usual parameters (1000 °C, 3-7×10^{-6} mbar oxygen pressure) to let the surface atoms relax to their most stable configuration. In case additional depositions have been performed [outcome (2) or (3) in the LEED measurement] one has to go back one step in the flowchart depicted in Figure 4.2,

and perform a new LEED measurement to check whether the correct amount has been deposited this time to end up with a (4×1)-(5×1)-reconstructed surface.

Finally, the sample surface is examined on a nanoscopic scale by performing STM. In case the surface is rough, shows many defects or is contaminated, it has to be sputtered and reprepared, as indicated in Figure 4.2. Otherwise, the *in-situ* preparation is finished and a sufficiently flat and well-ordered surface is obtained, which is terminated by the (4×1) and (5×1) reconstructions coexisting at the same time. Figure 4.3(e) shows a large-scale image of a flat surface whereas (f) depicts the corresponding small-scale image, revealing a well-ordered surface with a sufficiently low number of defects and surface contaminants. Furthermore, one can see separated domains terminated by the (4×1) and (5×1) reconstructions, which are highlighted in blue and red, respectively, in half of the image shown in Figure 4.3(f). Such prepared Nb-doped STO(110)-(4×1)-(5×1)-reconstructed samples are used as starting points for the homoepitaxial growth experiments presented in the following.

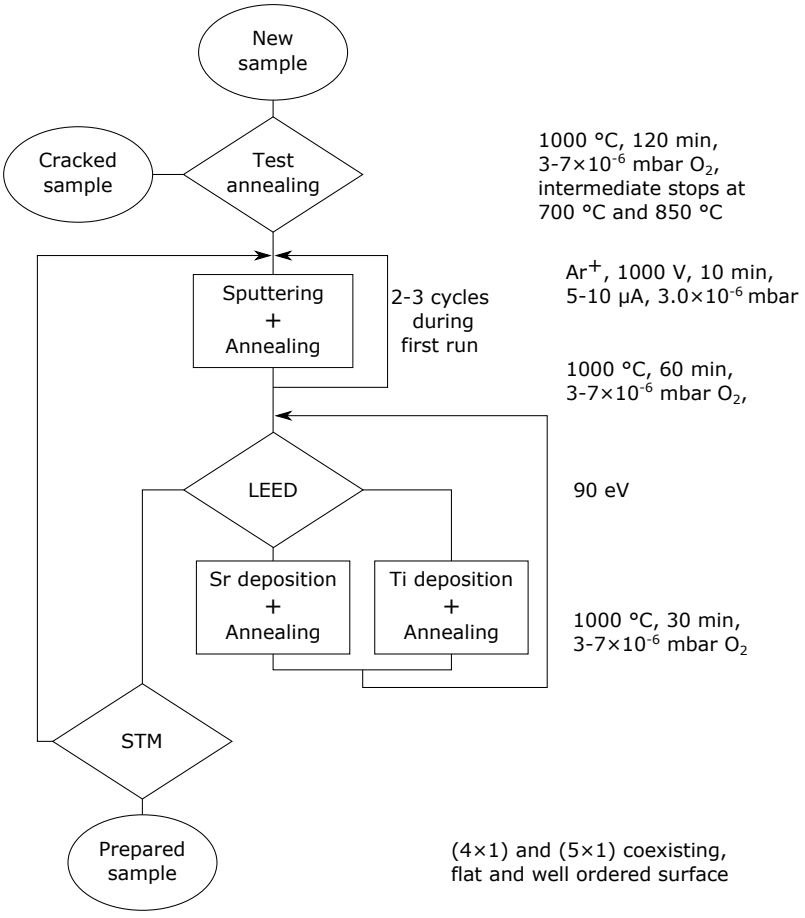

FIGURE 4.2: Flowchart of the *in-situ* sample preparation.

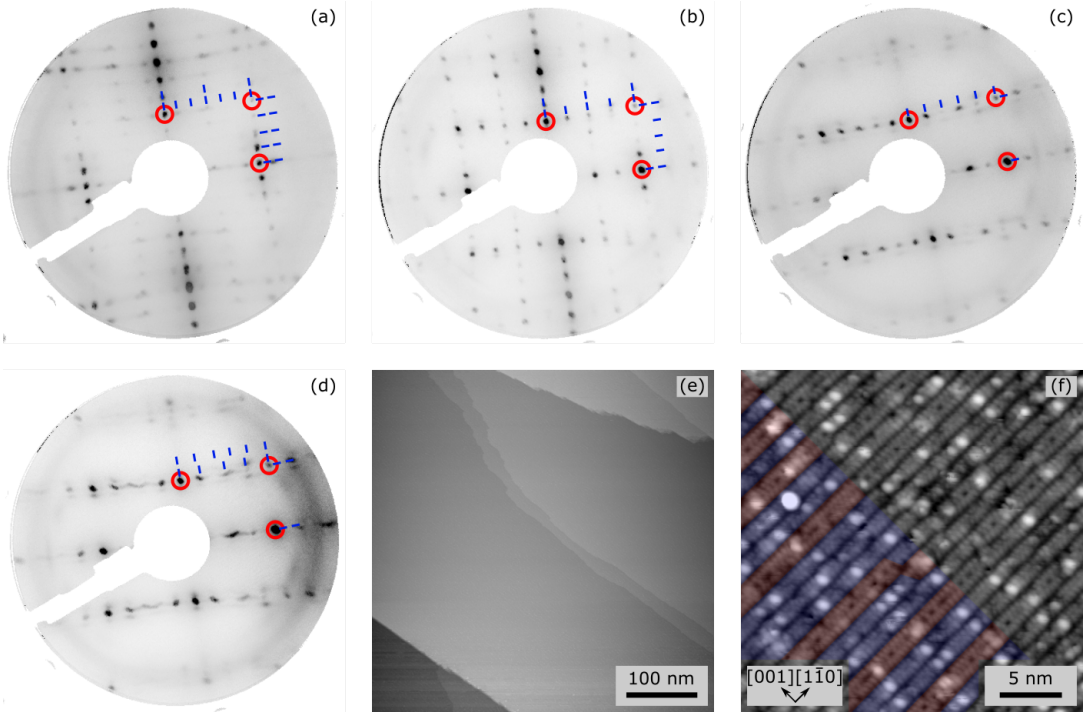

FIGURE 4.3: LEED and STM images during sample preparation: The bulk unit cell in the LEED images is marked by the red circles. The periodicities of the surface reconstructions are indicated by the blue bars. (a) LEED after 3 cycles of sputtering and annealing, revealing (6×4) and (2×4) reconstructions. (b) LEED pattern of a (4×1)-(2×4)-reconstructed surface, which is obtained after too little Sr has been deposited. (c) LEED pattern of a (5×1) surface, which is obtained after too much Sr has been deposited. (d) LEED pattern of a well-prepared surface consisting of (4×1) and (5×1) reconstructions at the same time. (e) Large-scale STM image (500×500 nm^2) revealing a flat surface. (f) 28×28 nm^2 STM image revealing a well-ordered, (4×1)-(5×1)-reconstructed surface. Both (4×1) and (5×1) form rows along the [1$\bar{1}$0] direction and can easily be distinguished from each other, as highlighted in blue and red, respectively, in half of the image.

4.3 Homoepitaxial growth of $SrTiO_3$ by means of PLD

This section is dedicated to the homoepitaxial growth experiments of Nb-doped $SrTiO_3$(110), which are the main experiments performed within this thesis. The growths were performed by PLD technique, using Nb-doped STO(110) samples as substrates, which had been prepared by the procedure explained above, so that their surface was sufficiently flat and terminated by the (4×1) and (5×1) reconstructions coexisting at the same time. All the growths were characterized by the same set of parameters, except for the fluence of the ablation laser, which is shown to determine the stoichiometry of the grown film.

Before performing each of the growth experiments a characterization of the pristine

surface was performed - comprised of LEED using 90 eV electrons, RHEED using 35 keV electrons, XPS using aluminum K_α radiation, and STM. STM images at different scales were acquired for different purposes: Large-scale images (500×500 nm^2) mainly provide information about the surface morphology in terms of flatness and presence of steps and islands, while small-scale images (70×70 nm^2 and smaller) allow to distinguish between domains of different surface reconstructions, as shown in Figure 4.3(f). By providing multiple STM images one can estimate the relative amounts of specific surface reconstructions by evaluating the area represented by that one specific reconstruction, and dividing it by the total area imaged.

The homoepitaxial growth experiments of STO were then performed in the PLD chamber according to the detailed description given in Section 3.7. They were designed in such a way that the fluence of the ablation laser was the only parameter to be varied in an interval ranging from 1.66 to 3.90 J/cm^2 (at the position hitting the target) by adjusting the power of single laser pulses. The dimensions of the 0.7×1.7 mm^2 rectangularly shaped spot on the target remained almost unchanged throughout the experiments. To determine the fluence accurately the spot size was measured with higher precision, using an optical microscope. The other parameters such as, *e.g.*, background pressure (5×10^{-6} mbar oxygen environment), substrate temperature (750 °C), target-substrate-distance (5.5 cm), and repetition rate of the laser pulses (1 Hz) were all kept constant. Additionally, the targets were preablated under growth conditions before each of the deposition experiments in order to remove possible surface contamination and to provide a reproducibly prepared target surface.

The growth processes were live-monitored by measuring the RHEED intensity of the specularly diffracted beam. Within the range of laser fluences used in our experiments always nice oscillations were observed, meaning that the growth proceeds in a layer-by-layer fashion (Frank-van der Merwe mode). The amplitude of these oscillations however decreased in time, possibly indicating that the composition of the deposited material did not perfectly match the bulk stoichiometry of STO. Under the assumption that the film grows stoichiometric, off-stoichiometries in the deposited material accumulate on the surface and could cause a decrease in RHEED intensity after each completion of a monolayer. A method in quantifying the off-stoichiometries within depositions based on that assumption is presented in Section 4.4. The experiments were characterized by depositing films with thicknesses ranging from 15 to 52 ML in total, corresponding to the same number of oscillations

in the RHEED signal. The growth processes were stopped manually by turning off the ablation laser once the last monolayer was fully completed, corresponding to a local maximum in the RHEED intensity. After the growth had been finished each sample was still kept at 750 °C for additional 10 min to let the surface atoms rearrange and heal possible defects.

Finally, surface characterization on the as-grown homoepitaxial films was performed, consisting of LEED, RHEED, XPS and STM, to document each individual growth, and allow to compare the results with the pristine surface. Based on the value of the laser fluence used for the growth, one can distinguish between two different types of growths in terms of surface morphology, which will be presented in Sections 4.3.1 and 4.3.2. In Section 4.4 it will be shown that the fluence affects the stoichiometry and that the two different types of growths correspond to slightly Ti-rich growths and slightly Sr-rich ones, respectively.

4.3.1 Titanium-rich growths

In our experiments, Ti-rich films were obtained using laser fluences exceeding 2.05 J/cm^2. Here in this section the results of one particular growth experiment are presented, which illustrate the qualitative characteristic features of all the Ti-rich growths performed within this thesis.

Figure 4.4 shows a collection of surface analysis results documenting a particular growth experiment characterized by a laser fluence of 2.61 J/cm^2. Figures 4.4(a-c) correspond to a well-prepared pristine surface and show a large-, a medium-, and a small-scale STM image, respectively. The small inset in Figure 4.4(a) depicts the LEED pattern of the sample before growth, indicating that the surface is terminated by the (4×1) and (5×1) reconstructions, which can also be identified in the small-scale STM image, shown in Figures 4.4(c).

Figure 4.4(d) documents the RHEED monitoring of the growth of 52 ML by shooting 927 laser pulses in total onto the target. The oscillations in the signal correspond to a layer-by-layer growth, and the decrease in amplitude indicates that the growth according to this mode is not stable over a long period of time. A possible reason for this observation is that the film does not grow perfectly stoichiometric. The fact that the RHEED intensity still raises after the growth has already stopped is explained by the fact that the sample was kept at the deposition temperature of 750 °C for an additional 10 min to allow rearrangement of the surface atoms; as the

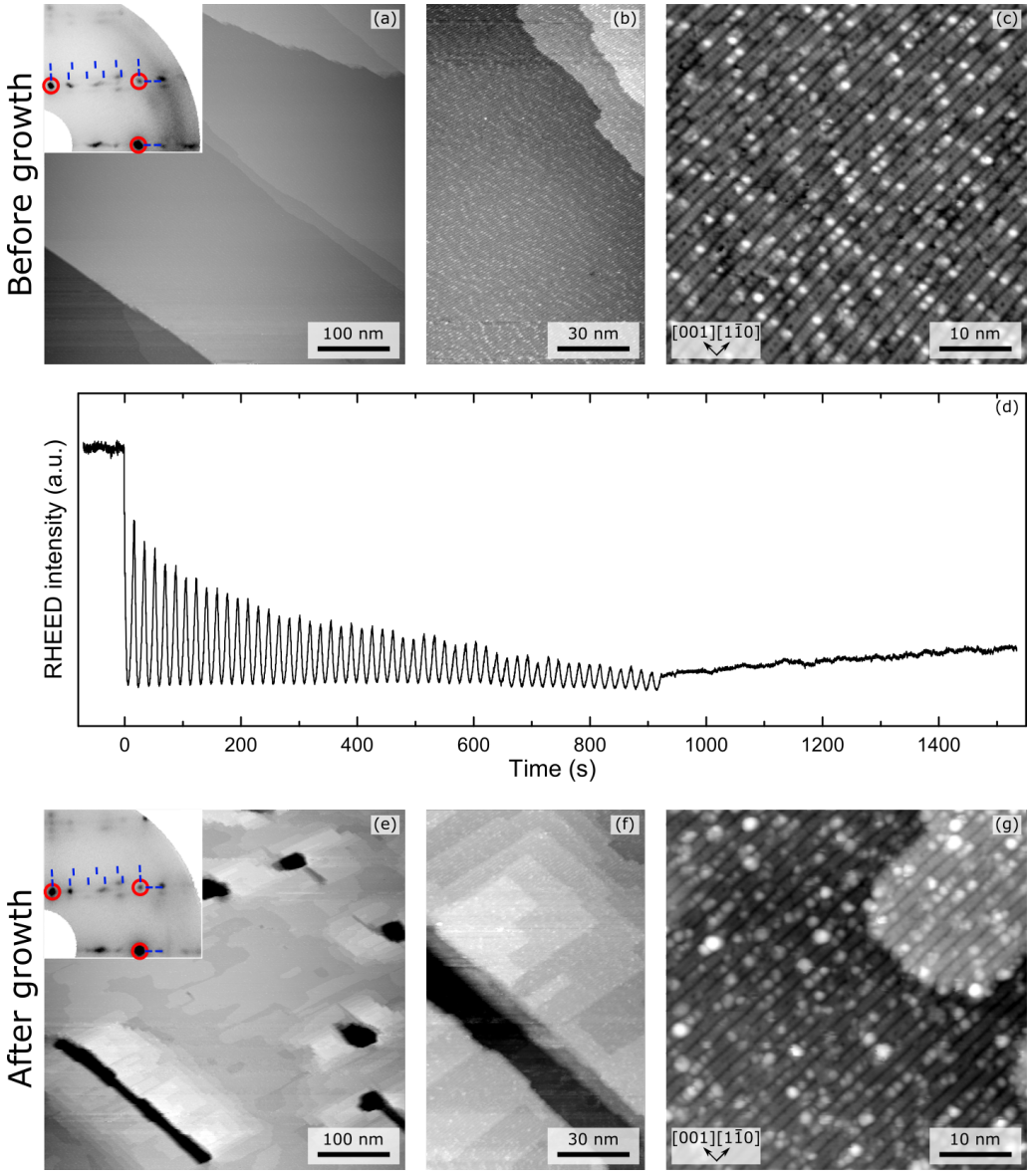

FIGURE 4.4: Collection of images documenting a Ti-rich growth characterized by a fluence of 2.61 J/cm^2. Panels (a-c) represent the surface before the growth. (a) Large-scale (500×500 nm^2) STM image and LEED pattern as an inset in the top left corner. (b) Medium-scale (91×150 nm^2) STM image. (c) Small-scale (50×50 nm^2) STM image. (d) RHEED monitoring of the intensity of the specularly diffracted beam during growth of 52 monolayers. Panels (e-g) represent the surface after the growth. (e) Large-scale (500×500 nm^2) STM image and LEED pattern as an inset in the top left corner. (f) Medium-scale (91×150 nm^2) STM image. (g) Small-scale (50×50 nm^2) STM image.

surface gets flatter, the RHEED intensity recovers [20].

Figures 4.4(e-g) show the surface analysis result of the same sample after the deposition of 52 ML of Nb-doped STO. Figure 4.4(e) depicts a large-scale STM image and the LEED pattern as an inset, Figure 4.4(f) shows a medium-scale STM image, and Figure 4.4(g) shows a small-scale STM image of the surface. When just by

comparing the LEED and RHEED results before and after the growth, one would not expect significant changes in the surface morphology, since in both cases a combination of (4×1) and (5×1) patterns are observed. However, the STM images in Figures 4.4(e-g) show that the surface morphology has changed as a new feature appeared that was not present on the pristine surface, namely pits. Most of the pits are elliptically shaped with lengths in between 40 and 100 nm, and widths between 15 and 40 nm. However, there are outliers in the pit statistics as well, as for example the 250×25 nm^2 pit, shown in Figure 4.4(e). Based on line scans the depth of the pits is estimated to lie in a range from 2 to 10 nm. Since the bottom parts of the pits were not well imaged in most of the cases, as, *e.g.*, double tip effects are more likely to occur while imaging such rough regions, the results of our depth measurement have to be treated with caution.

A medium-scale STM image and a line scan of a pit are shown in Figures 4.5(a) and (b), respectively. A closer inspection of the pits reveals that there are rows of a smaller periodicity present at their bottom, as shown in Figures 4.4(c). In fact, these structures can be assigned as (2×4), as shown by Gerhold [10]. This fact also provides a possible explanation of how the pits were created: While depositing slightly Ti-rich STO, the Ti excess pushes the surface towards titanium-rich reconstruction, which is equivalent to a movement to the right in the surface phase diagram, depicted in Figure 1.2. In our particular experiments we start from (4×1)-(5×1)-reconstructed surfaces, and the slight excess of Ti within the deposited material is used to partly transform (5×1) to (4×1) and (4×1) to (2×4), respectively. Previous experiments have shown that (2×4) is characterized by a lower sticking probability compared to (4×1)-(5×1). Therefore, it can be concluded that the growth on the (4×1)-(5×1)-reconstructed area proceeds faster compared to the (2×4)-reconstructed one, resulting in the formation of pits.

Figure 4.6 depicts the results of the XPS analyses belonging to the same growth experiment that is documented in Figure 4.4. Figure 4.6(a) shows a full-energy-range survey spectrum, with its main peaks labelled, and Figure 4.6(b) and (c) show the detailed spectra of the Ti 2p and Sr 3d peaks, respectively. Within these spectra curve (1) belongs to the pristine sample, whereas (2) was measured after the homoepitaxial deposition of 52 ML Nb-doped STO. In both the spectra before and after the growth tiny signals of contamination are present located at binding energies of 203.8 eV (Nb 3d) and 736.2 eV (unidentified peak, labelled as * in Figure 4.6). The Nb signal however is expected since both the pristine substrate as well as the

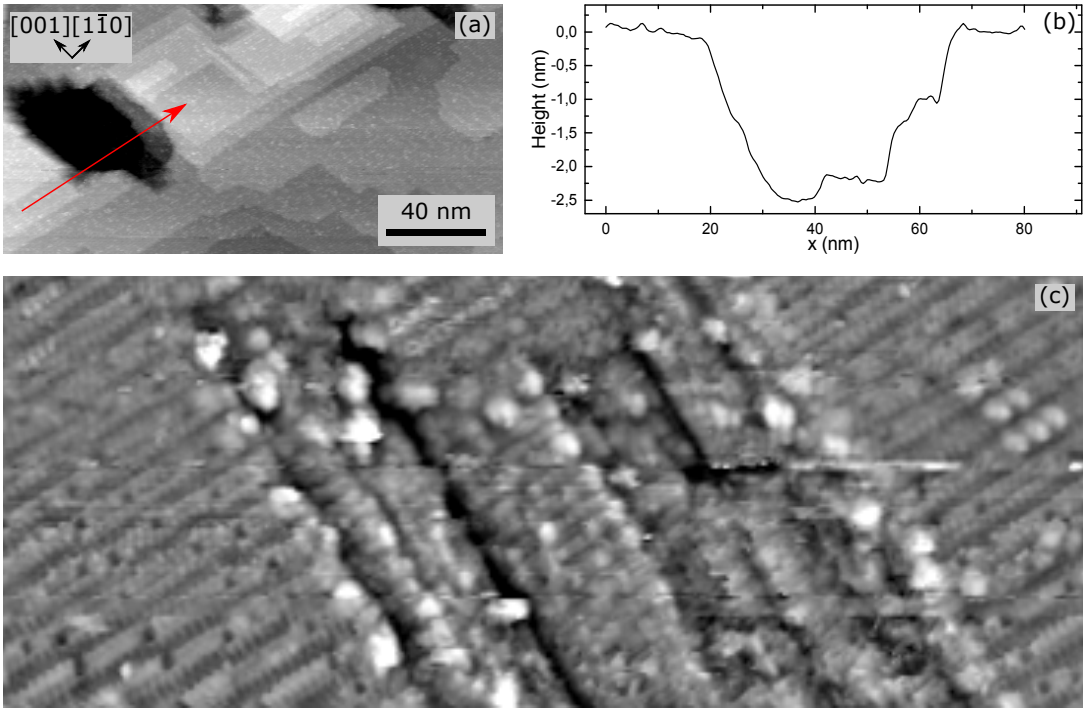

FIGURE 4.5: Characteristic features of pits. (a) Medium-scale STM image (200×100 nm^2) of a pit of approximate size of 60×40 nm^2. (b) Line profile along the vector shown in (a). (c) High-pass filtered 50×20 nm^2 STM image of a pit. In the center of the image (2×4) reconstructions can be identified at the bottom of the pit. The scratches and imaging errors, *e.g.* double tip effects, in parts of this image indicate that it is difficult to acquire nice images of the bottom part of pits.

material used for the deposition were 0.5 wt.% Nb-doped. Based on the XPS results it is possible to estimate eventual off-stoichiometries in the film by comparing the relative intensities before and after the growth, as described in Section 4.5 in more detail. The main conclusion from these evaluations was that the off-stoichiometries of the films grown within this thesis are below the detection limit of XPS, which is about 2%.

In an additional experiment, a Ti-rich grown film was annealed for 1 hour at a temperature of 1000 °C in 3-7×10^{-6} mbar oxygen environment in order to study the effects of the annealing on the sample surface. A summary of the STM results is depicted in Figure 4.7. It has to be noted that the images shown in Figure 4.7 do not refer to the same sample that is documented in Figure 4.4, but its surface before the annealing was equivalent, as it was characterized by (4×1) and (5×1), and by the presence of pits. By comparing the qualitative results in the large-scale STM images before and after annealing, shown in Figure 4.4(e) and Figure 4.7(a), respectively, one can see that the annealing supports the ordering process. The terraces now are larger and they have predominantly straight edges along the main

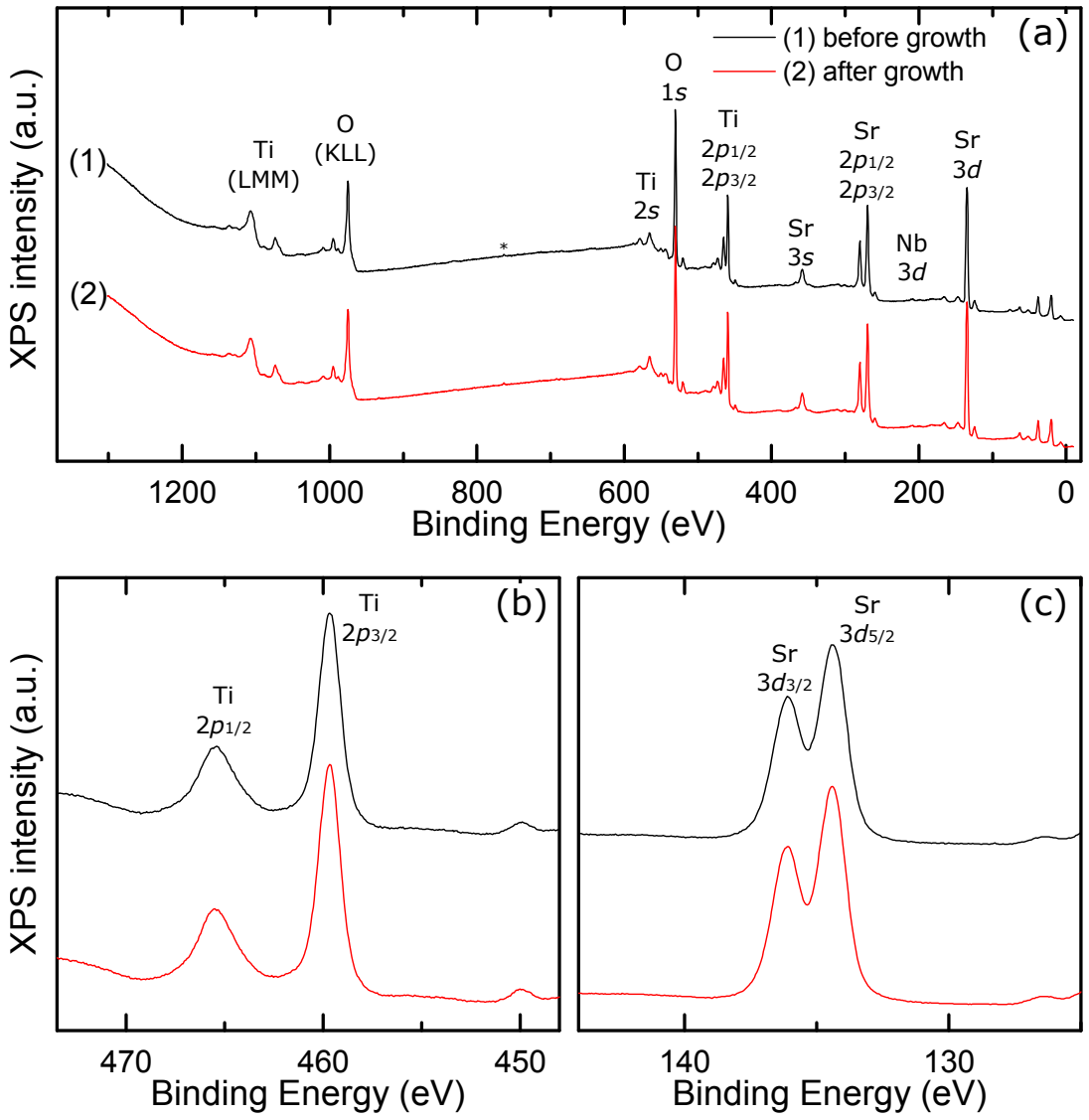

FIGURE 4.6: XPS analysis of the slightly Ti-rich grown film, documented in Figure 4.4. (a) Full-energy-range survey scan. (b) Detail of the Ti $2p$ peaks. (c) Detail of the Sr $3d$ peaks. Curve (1) was acquired from the pristine sample whereas curve (2) represents the spectrum of the slightly Ti-rich grown film. Each spectrum is normalized to the intensity of the O $1s$ peak, after subtraction of a Shirley-type background. The X-ray source supplied aluminum K_α radiation (1486.6 eV). The pass energy of the detector was set to 50 eV for the full energy survey in (a) and 10 eV for the detailed spectra in (b) and (c).

crystallographic axes. The same holds true for the pits, which are almost perfectly rectangularly shaped. A closer inspection reveals that there are smaller terraces along the step edges, which are characterized by a different type of surface reconstruction, as highlighted by the yellow colouring in the medium-scale STM image in Figure 4.7(b).

The 50×50 nm^2 STM image in Figure 4.7(c) shows that such domains are charac-

terized by the (2×4) reconstructions (highlighted in yellow), while the majority of the surface is determined by (4×1). In conclusion, annealing at 1000 °C caused the surface to transform from being (4×1)-(5×1)-(2×4) to (4×1)-(2×4), while the pits stayed present and only changed in shape. Such a change in surface reconstructions is corresponding to a Ti enrichment of the surface according to the surface phase diagram of STO(110) in Figure 1.2. A detailed discussion of possible reasons for this behaviour is given in Section 4.5.

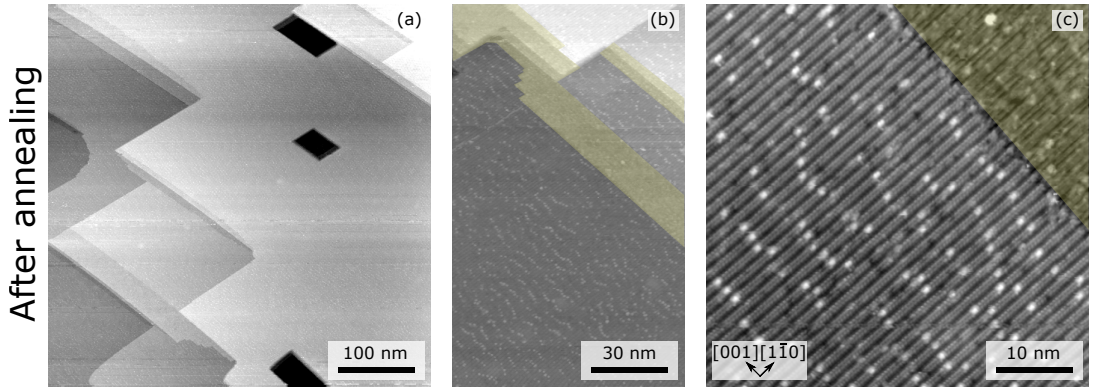

FIGURE 4.7: Effect of annealing (1000 °C, 1 h, 3-7×10^{-6} mbar O_2) on a Ti-rich grown film, characterized by a laser fluence of 2.09 J/cm^2. Note that the results shown here do not correspond to the same film documented in Figure 4.4. (a) Large-scale (500×500 nm^2) STM image. (b) Medium-scale (91×150 nm^2) STM image. (c) Small-scale (50×50 nm^2) STM image. Areas, which are covered by (2×4) reconstructions, are highlighted in yellow in (b) and (c), respectively.

4.3.2 Strontium-rich growths

In our experiments, Sr-rich films were obtained using laser fluences below 2.05 J/cm^2. As an illustration of slightly Sr-rich growths in general, the surface analysis results of one particular experiment are presented in this section.

Figure 4.8 shows a collection of images documenting the growth of a 15 ML-thick Nb-doped STO film, characterized by a laser fluence of 1.93 J/cm^2 for the deposition. Figures 4.8(a-c) show a large-scale, a medium-scale, and a small-scale image of the well-prepared sample before the growth. The inset in (a) depicts the LEED pattern of the pristine sample, revealing both (4×1) and (5×1) periodicities in the surface reconstructions. Figure 4.8(d) depicts the RHEED monitoring of the specularly diffracted beam during the deposition plus 10 min of post-annealing. This growth is characterized by oscillations of decreasing amplitudes, similar to the RHEED monitoring of the slightly Ti-rich grown film, shown in Figure 4.4(c), and in order

to compare the results, both curves are normalized to the same initial intensity. One can see that the growth rates were different for these two experiments, which is explained by the fact that that different fluences were used for the depositions, while all the other parameters, especially the repetition rate of the laser pulses, were chosen to be the same. The Ti-rich deposition shown in Figure 4.4(c) consisted of 266 pulses to deposit the first 15 ML, whereas 354 pulses were needed to deposit the same number of monolayers for the Sr-rich deposition in Figure 4.8(c). A more detailed discussion of the dependence of the growth rate on the laser fluence is found in Section 4.5, where the results of all the growths performed within this thesis are compared. Figures 4.8(e-g) depict a set of STM images of different sizes, taken after the deposition of the 15 ML-thick Sr-rich film, revealing a rather flat and well-ordered surface, sparsely covered by small 1 ML-high islands. The presence of such islands is most likely explained by the fact that the deposition process was stopped slightly after, rather than exactly when, the last monolayer was completed. In the small-scale STM image [Figure 4.8(g)] rows corresponding to both (4×1) and (5×1) surface reconstructions are identified, which is consistent with the LEED results, shown as insets in Figure 4.8(e) and (g), respectively. Closer inspection yields that after the growth (5×1) is present in a larger proportion compared to the pristine surface, which was predominantly determined by (4×1) [cfr. Figure 4.8(c) and Figure 4.8(g)]. According to the surface phase diagram of STO(110) in Figure 1.2, such a change in surface reconstructions is explained by a slightly off-stoichiometric growth characterized by Sr excess.

In order to study thermal effects on the surface structures of a Sr-rich grown film, the particular one that is documented in Figure 4.8 was annealed for 4 hours at 1000 °C in 3-7×10^{-6} mbar oxygen environment. The surface analysis results comprising STM and the LEED are shown in Figure 4.9. Figure 4.9(a) exhibits a large-scale STM image, revealing a flat and well-ordered surface, and the LEED pattern in the upper left corner indicates a (4×1)-(5×1)-reconstructed surface. By comparing the large-scale STM images before [Figure 4.8(e)] and after annealing [Figure 4.9(a)] one can see that all the islands have disappeared due to surface diffusion processes. Even though this particular Sr-rich film was annealed longer (4 h) than the Ti-rich film in Figure 4.7(a) (1 h), the terrace edges are not as well oriented along the main crystallographic axes. This can be explained by the fact that the surface reconstructions are different. Whereas the Sr-rich film is characterized by (4×1) and (5×1) the Ti-rich film is terminated by (4×1) and (2×4). Figures 4.9(b) and

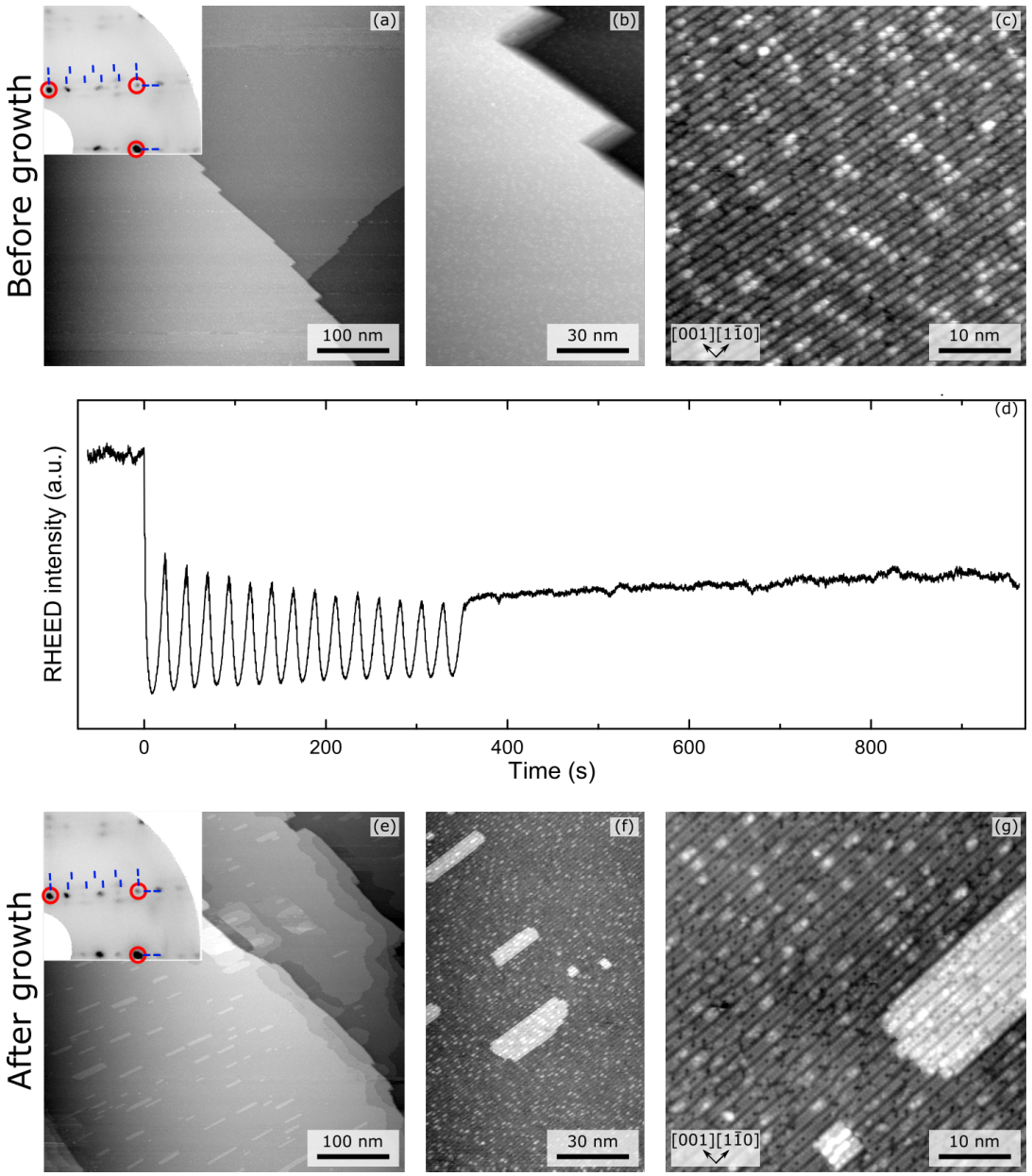

FIGURE 4.8: Collection of images documenting a Sr-rich growth characterized by a fluence of 1.93 J/cm^2. Panels (a-c) represent the surface before the growth. (a) Large-scale (500×500 nm^2) STM image and LEED pattern as an inset in the top left corner. (b) Medium-scale (91×150 nm^2) STM image. (c) Small-scale (50×50 nm^2) STM image. (d) RHEED monitoring of then intensity of the specularly diffracted beam during growth. Panels (e-g) represent the surface after the growth of 15 monolayers. (a) Large-scale (500×500 nm^2) STM image and LEED pattern as an inset in the top left corner. (b) Medium-scale (91×150 nm^2) STM image. (c) Small-scale (50×50 nm^2) STM image.

(c) represent a medium- and a small-scale STM image of the annealed Sr-rich film, respectively, confirming that the surface is indeed (4×1)-(5×1) reconstructed. By having a close look on small-scale STM images before and after the annealing [cfr. Figure 4.8(g) and Figure 4.9(c)], one notices that, even though both surfaces are

represented by (4×1)-(5×1), the relative amount of (4×1) has increased through the annealing process. Based on the information given by the surface phase diagram in Figure 1.2 it can be concluded that an annealing process comes with a Ti enrichment of the surface. This is consistent with the effects of an annealing process on a Ti-rich film, as described in Section 4.3.1.

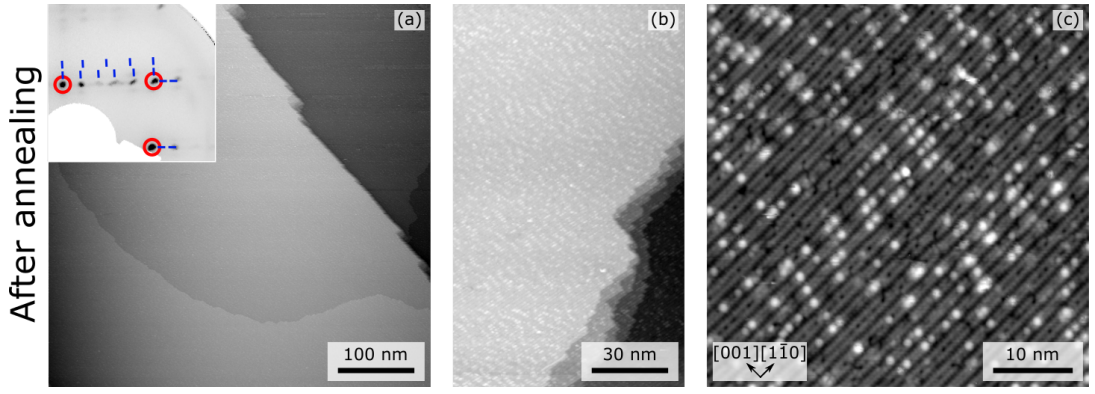

FIGURE 4.9: Effect of annealing (1000 °C, 4 h, 3-7×10^{-6}mbar O_2) on a Sr-rich grown film. The results in this figure correspond to the same film that is documented in Figure 4.8. (a) Large-scale (500×500 nm^2) STM image and LEED pattern as an inset in the top left corner. (a) Large-scale (500×500 nm^2) STM image. (b) Medium-scale (91×150 nm^2) STM image. (c) Small-scale (48×48 nm^2) STM image.

In addition to the previously discussed Nb-doped growths, a 15 ML-thick undoped STO(110) film was deposited onto a Nb-doped STO(110) substrate. After analysing the film, the surface was prepared to be (4×1)-(5×1) reconstructed (deposition of Sr and Ti, respectively, followed by annealing) such that it functioned as a new substrate for further growths of undoped STO(110). All these growths were performed using low fluences corresponding to the Sr-rich regime, while the other parameters were chosen to be the same as in the previous experiments (see Section 4.3). The growths of undoped STO(110) were characterized by nice oscillations in the RHEED signal and possibly due to oxygen vacancies within the film the electric mobility was sufficient to be able to perform STM. The STM results of the films of undoped STO(110) were qualitatively the same as the ones of the Nb-doped films characterized by (4×1) and (5×1) [see Figure 4.8(e)-(g)], and are thus not shown.

4.4 Quantification of the stoichiometry via STM

In order to quantify the off-stoichiometries within our homoepitaxial growth experiments of STO(110), a method was developed that is based on the statistical

evaluation of the areal composition of the respective surface reconstructions in the STM images, before and after the deposition, and combining these results with the information given by the STO(110) surface phase diagram [Figure 1.2]. First, this method is introduced under theoretical aspects and it is shown that it can be applied for homoepitaxial growth experiments of STO. In the following this model is applied to evaluate the off-stoichiometries of the growths performed within this thesis. Based on these results it was possible to identify the regimes in fluence of the ablation laser used for the PLD processes causing either slightly Ti-rich or slightly Sr-rich films, respectively.

Idealized model

Ideally, this method can be used to determine the off-stoichiometry of any homoepitaxial growth experiments that meet several conditions, which are explained in the following. The first three conditions are requirements concerning materials that are used for such experiments, whereas the fourth is referring to how the homoepitaxial growth process is taking place. (1) Both the surface of the pristine substrate as well as the surface of the grown film have to exhibit at least two different surface reconstructions coexisting at the same time, whose composition is profoundly related to the local stoichiometry. Within this context these reconstructions are referred to as A and B, as also shown in Figure 4.10(a). (2) These surface reconstructions have to have the property that they can be tuned reversibly by introducing off-stoichiometries. Stated differently, it has to be possible to transform reconstruction A to B by depositing a certain material, referred to as material 1. Additionally, it has to be possible to transform B to A by depositing a different material, referred to as material 2. (3) The transitions from A to B and *vice versa* have to take place in a reproducible manner. This means that always the same amount of a certain material has to be deposited to tune a certain amount of A to B. Same holds true for the transition B to A. (4) When growing several monolayers homoepitaxially it is assumed that the film grows according to the bulk stoichiometry, and eventual off-stoichiometries in the deposited material cause only a change in the composition of surface reconstructions.

The basic ideas behind this model are illustrated in Figure 4.10 both from a theoretical point of view, as well as in terms of actual growth experiments of STO(110). The theoretical aspects of this approach, which are shown in Figure 4.10(a) and (b), are discussed first. With all the previously stated conditions being met, a reference experiment has to be performed first, which is illustrated in Figure 4.10(a). This

reference experiment consists of preparing a surface that it is purely terminated by reconstruction A and then determining the exact amount of off-stoichiometries, referred to material 1, that one has to deposit to end up with a surface that is purely terminated by reconstruction B. This experiment has to be performed the other way as well, starting from a purely B-terminated surface and determining the exact amount of material 2 that has to be deposited to tune the surface to the purely A-terminated one. Additionally, it has to turn out that these reference experiments deliver reproducible results, as required by condition (3). Within the procedure explained in this section, the off-stoichiometries of a general homoepitaxial growth, schematically represented by Figure 4.10 (b), can then be derived from the results of the reference experiments. This general growth however has to fulfil condition (4), meaning that the film grows perfectly stoichiometric while the off-stoichiometries accumulate on the surface and cause a relative change in the surface reconstructions. Furthermore, the growth experiment has to be well documented, such that areal composition of the respective surface reconstructions, both before and after the growth, can be evaluated precisely. By this means the relative change in surface reconstructions through the deposition process can then be calculated and, by combining this result with the information obtained in the reference experiment, the total amount of off-stoichiometries introduced during the growth can be derived. In case the total amount of deposited material, *e.g.*, the number of monolayers deposited, is known, a normalized off-stoichiometry parameter can be calculated by dividing the total off-stoichiometry by the number of monolayers.

Application to STO(110)

In the following it is shown that the STO(110) meets the conditions that are required to use this general approach to determine off-stoichiometries in a homoepitaxially grown film. As presented in Chapter 1 and illustrated in the surface phase diagram [Figure 1.2], STO(110) exhibits a whole series of different surface reconstructions, which determine the local, near-surface stoichiometry. Furthermore, the STO(110) surface does have the property that it can be tuned by depositing precise amounts of Ti and Sr, respectively, and such a surface tuning is reproducible as well. Therefore, conditions (1) - (3) are fulfilled. Due to the fact that the growth experiments presented in this thesis are characterized by a layer-by-layer mode (Frank-van der Merwe) it is assumed that the surface adatoms have enough time to arrange such that the film is growing according to the bulk lattice structure, and the 10 min of post-annealing at the deposition temperature should support such an equilibration

as well. However, it was shown that the surface termination of the films slightly changes through a further annealing at 1000 °C, which is a higher temperature compared to the substrate temperature during the deposition (750 °C). This means that condition (4) is met approximately only, and when interpreting the results this fact has to be taken into account. Furthermore, it has to be possible to determine the precise areal composition of the different surface reconstructions. Within this thesis two different techniques were used for that purpose: LEED was used first to get a rough estimate, which surface reconstructions were present, and then STM was performed to do a precise evaluation.

The method of determining off-stoichiometries in actually grown homoepitaxial films of STO(110) is discussed in the following and illustrated in Figures 4.10(c) and (d) featuring small-scale STM images. For the sake of simplification and in order to stress the analogies to the theoretical approach [see Figures 4.10(a) and (b)] only the (4×1) and (5×1) surface reconstructions are considered, and are highlighted in blue and red, respectively. Figure 4.10(c) depicts a reference experiment, which is used to determine the amount of off-stoichiometries, here Sr and Ti, that one has to deposit to cause a transition from pure (4×1) to pure (5×1), and *vice versa*. Figure 4.10(d) shows a comparison of STM images before and after a slightly off-stoichiometric homoepitaxial growth. Due to the fact that the areal share of (4×1) decreased, while the one of (5×1) increased, it can be concluded that the growth process is slightly Sr-rich, and the exact amount of off-stoichiometries can be be derived by evaluating the relative changes and set them in relation with the results from the reference experiment.

As already mentioned, STO(110) features a whole set of different surface reconstructions, and therefore it would be necessary to perform a whole series of reference experiments, one for each different transition between two purely terminated surfaces. Within this thesis however this was not required since the surface phase diagram of the STO(110) [see Figure 1.2] was used as a reference covering all this information. Therefore, it was just necessary to do the second part of this two-step procedure, which consisted of documenting the individual homoepitaxial growth experiments by a set of STM images each. Based on these images, statistics of the composition of the different surface reconstructions were obtained, and by calculating the relative changes and setting them in relation with the information given by the surface phase diagram the actual off-stoichiometries were calculated.

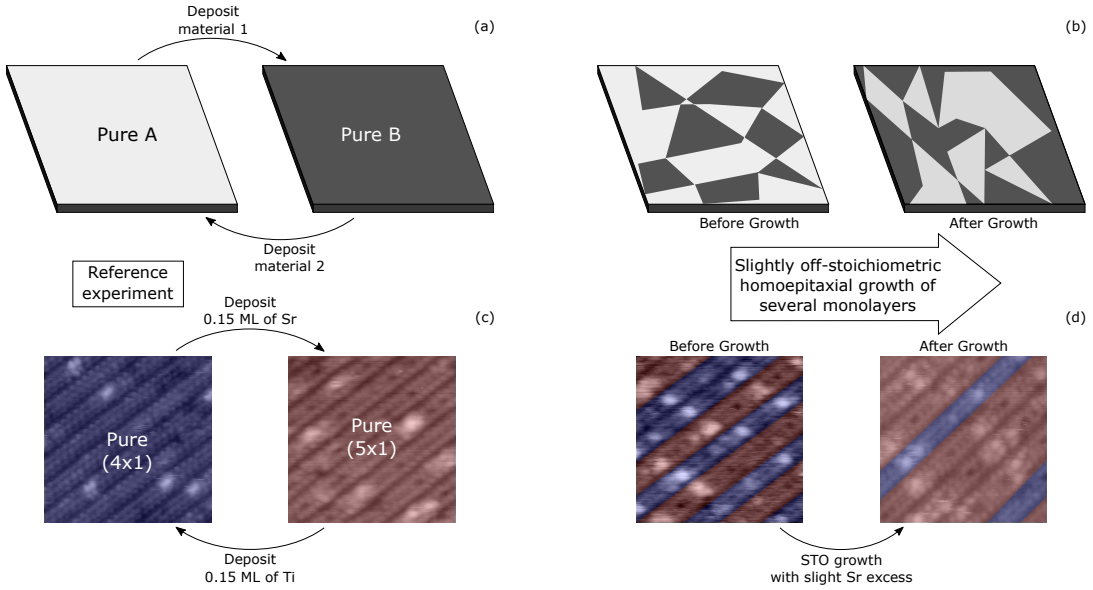

FIGURE 4.10: Model of quantifying off-stoichiometries by measuring a change in surface reconstructions. (a) Theoretical model of a reference experiment consisting of reversibly introducing off-stoichometries to induce a transition from surface reconstructions A to B, and *vice versa*. (b) Theoretical model of a slightly off-stoichiometric homoepitaxial growth and the relative change in surface reconstructions involved. (c) Small-scale STM images representing a reference experiment on the STO(110) surface considering only the (4×1) and (5×1) surface reconstructions. (d) Small-scale STM images documenting a slightly off-stoichiometric homoepitaxial growth of STO. The (4×1) and (5×1) reconstructions are highlighted by a blue and a red colouring, respectively.

Data evaluation of homoepitaxial STO(110) films

As presented in Sections 4.3.1 and 4.3.2 the surface morphology of the homoepitaxial films of STO(110) depends on the laser fluence used for the deposition as, *e.g.*, pits can be formed. For that reason, the precise surface characterization by means of statistical data evaluation has to be performed very carefully by treating special features like pits properly.

In general, before and after each individual deposition experiment a set consisting of 8 to 26 STM images (sizes in the range between 50×50 nm^2 and 100×100 nm^2) was acquired, providing the data for the precise characterization of the surface termination. The number of images per set was dependent on the size of the respective images, and was chosen such that a number between 600 and 1600 rows corresponding to the (4×1) and (5×1) reconstructions were imaged in total. Additionally, in case pits were present, a second set consisting of around 10 images (500×500 nm^2) was taken to provide further statistics on the area covered by the pits. In the following the exact procedure of evaluating the composition of the different surface reconstructions, and in turn the procedure of calculating the off-stoichiometries in

the film is shown.

In this paragraph, the procedure of determining the relative share of the different surface reconstructions of a well-prepared sample before the growth is presented. As shown in Figures 4.3(e) and (f), such a sample exhibits a flat surface, which is terminated by the (4×1) and (5×1) reconstructions only. For the evaluation of the areal composition of these two surface reconstructions we took advantage of the fact that they are forming well-defined rows. Instead of measuring the respective areas that are terminated by (4×1) and (5×1), respectively, just the corresponding number of rows was determined, providing all the required information to calculate the relative areal share. Within this process individual STM images functioned as samples, and the total number of (4×1) rows $N_{(4\times1)}$ as well as the number of (5×1) rows $N_{(5\times1)}$ were counted. In the next step, the relative areal share of the (4×1) reconstruction, $\theta^{\mathrm{b}}_{(4\times1)}$, was calculated for each individual image according to Equation 4.1. In this formula, the factors 4 and 5 take into account the different widths of the unit cells of the (4×1) and (5×1) reconstructions, and therefore the different widths of the observed rows. The superscript b indicates that this quantity describes the surface before the growth. Finally, the average value of $\theta^{\mathrm{b}}_{(4\times1)}$ as well as its standard deviation were calculated, using the data from individual STM images.

$$\theta^{\mathrm{b}}_{(4\times1)} = \frac{4 \times N_{(4\times1)}}{4 \times N_{(4\times1)} + 5 \times N_{(5\times1)}} \tag{4.1}$$

In order to evaluate the composition of the different surface reconstructions after growing a homoepitaxial film, a distinction in cases is necessary as surfaces of different morphology can be obtained, as shown in Sections 4.3.1 and 4.3.2. First, Sr-rich grown films are considered, which are characterized by a flat surface and are terminated only by the (4×1) and (5×1) reconstructions, as shown in Figures 4.4(e-g). These are exactly the same conditions that were met before the growths, and therefore $\theta^{\mathrm{a}}_{(4\times1)}$, representing the relative areal share of the (4×1) surface reconstructions after the growth, can be determined analogously to $\theta^{\mathrm{b}}_{(4\times1)}$ by using the same formula [see Equation 4.1]. Again, each individual STM image functioned as a sample, and based on these results an averaged value of this quantity plus its standard deviation were evaluated. Finally, Equation 4.2 provides a formula to calculate $\Delta^{\mathrm{total}}_{\mathrm{Ti}}$, representing the total amount of Ti off-stoichiometries in ML that are accumulated during the growth process. The factor 0.15 in this equation provides the information given by the surface phase diagram and represents the amount of ML of Ti

that one has to introduce to tune a purely (5×1)-terminated STO(110) surface to be purely (4×1)-reconstructed one. Note that Sr-rich grown films are characterized by a negative value of $\Delta_{\mathrm{Ti}}^{\mathrm{total}}$, meaning that there is a lack of Ti with respect to the stoichiometric composition.

$$\Delta_{\mathrm{Ti}}^{\mathrm{total}}(\text{Sr rich}) = (\theta_{(4\times1)}^{\mathrm{a}} - \theta_{(4\times1)}^{\mathrm{b}}) \times 0.15 \tag{4.2}$$

Next, Ti-rich grown films are considered, which are characterized by flat parts terminated by (4×1) and (5×1) reconstructions, as well as pits, as shown in Figures 4.4(e-g). In this case, the evaluation of the areal composition of the surface reconstructions was performed in two steps. Due to the fact that the pits were just sparsely spread on the surface, first a set of large-scale STM images (500×500 nm^2) was acquired with the purpose of determining the share of the area represented by pits, A_{P}, which corresponds to the relative fraction of (2×4), as shown in Figure 4.5. The evaluation of A_{P} was performed by using the software ImageJ and consisted of approximating the pits in the STM images by polygons, evaluating their area, and then dividing the total pit area by the size of the STM image. The second step consisted of acquiring images of higher magnification in order to evaluate the relative shares of the (4×1) and (5×1) surface reconstructions in the flat parts of the surface. Within this process the same procedure, as previously discussed, was used consisting of counting the respective rows. With these quantities being evaluated, the off-stoichiometries of Ti-rich grown films were calculated using Equation 4.3. This equation consists of two separate parts: The first part takes into account the share of the originally (4×1)-(5×1)-reconstructed area that is transformed into (2×4)-reconstructed pits, whereas the factors 0.75 and 0.90 correspond to the amount of Ti (in ML) that one has to introduce to achieve such a surface tuning, as given by the surface phase diagram [Figure 1.2]. The second part describes the relative change in surface reconstructions in the flat part (non-pit area) where only the ratio between (4×1) and (5×1) changes. Therefore, this term is proportional to the expression in Equation 4.2.

$$\begin{aligned}\Delta_{\mathrm{Ti}}^{\mathrm{total}}(\text{Ti rich}) = A_{\mathrm{P}} \times [(\theta_{(4\times1)}^{\mathrm{b}} \times 0.75 + (1 - \theta_{(4\times1)}^{\mathrm{b}}) \times 0.90] + \\ +(1 - A_{\mathrm{P}}) \times (\theta_{(4\times1)}^{\mathrm{a}} - \theta_{(4\times1)}^{\mathrm{b}}) \times 0.15\end{aligned} \tag{4.3}$$

In both of the cases, Sr-rich films and Ti-rich films, the uncertainties of the off-

stoichiometry parameter $\Delta_{\mathrm{Ti}}^{\mathrm{total}}$ were estimated by linear error propagation. In order to be able to compare the off-stoichiometries of films of different thicknesses, a dimensionless Ti off-stoichiometry parameter Δ_{Ti} is introduced, which is defined in Equation 4.4 with N_{ML} representing the total number of monolayers that were deposited within the experiment. This dimensionless Ti off-stoichiometry parameter is a quantity, which gives information about the Ti off-stoichiometries in ML (excess and lack, respectively) that are introduced by growing exactly 1 ML STO. Equivalently, it can also be interpreted as the relative amount of Ti off-stoichiometries in the film, in the hypothesis that all the off-stoichiometries float to the surface.

$$\Delta_{\mathrm{Ti}} = \Delta_{\mathrm{Ti}}^{\mathrm{total}} / N_{\mathrm{ML}} \tag{4.4}$$

4.5 Comparison of the results

This section comprises the results of the statistical analysis concerning the homoepitaxial growth experiments. First, off-stoichiometries derived from the XPS analyses are presented, showing that eventual off-stoichiometries have to be below the detection limit of XPS. Then the values of the off-stoichiometries, which were obtained by the method using STM images, described in Section 4.4, are presented.

In order to estimate the off-stoichiometries within the individual growth experiments by means of XPS, detailed spectra of the Ti $2p$ peaks and the Sr $3d$ peaks were acquired, both before and after the homoepitaxial deposition of STO, as shown in Figure 4.6(b) and (c) for example. Next, the areas of these peaks, representing their intensity I, plus their uncertainties were evaluated, after subtraction of a Shirley-type background. In a final step, the ratio of the relative intensities, RRI, was calculated for each experiment, using Equation 4.5, and its uncertainty was determined by linear error propagation. The subscripts a and b in Equation 4.5 indicate that the respective intensities have to be evaluated from the spectra taken after and before the deposition, respectively. The quantity RRI can be considered as a dimensionless off-stoichiometry parameter, which is greater than one for Ti-rich growths, and smaller than one for Sr-rich growths. A growth characterized by RRI=1 is considered to be perfectly stoichiometric, within the uncertainties of this particular method.

$$RRI = \frac{\left(\frac{I(\text{Ti } 2p)}{I(\text{Sr } 3d)}\right)_{\text{a}}}{\left(\frac{I(\text{Ti } 2p)}{I(\text{Sr } 3d)}\right)_{\text{b}}} \tag{4.5}$$

Figure 4.11 shows the RRI values of some of the growths performed within this thesis as a function of the laser fluence. Due to the fact that the line RRI=1 lies inside the error bar of each individual point, a high degree of stoichiometry can be concluded. Furthermore, because all the data points are located so close together such that their error ranges overlap, it is not possible to assign significant differences in the change of stoichiometry throughout the experiments. In case there were any changes, they had to be smaller than the detection limit of this method, which is essentially defined by the length of the error bars and has a numeric value of around 2 %.

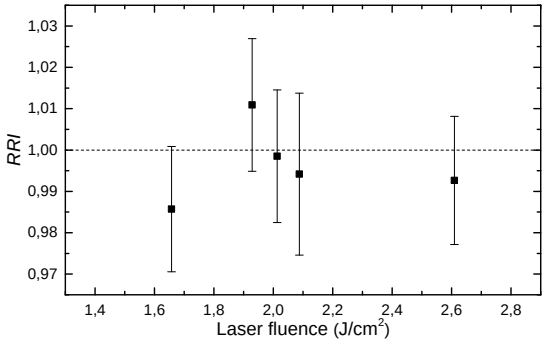

FIGURE 4.11: Ratio of the relative XPS intensities (RRI), as defined in Equation 4.5, as a function of the laser fluence of the respective growths. The dashed horizontal line corresponds to perfectly stoichiometric growths, while RRI>1 indicates Ti-rich growths and RRI<1 Sr-rich growths, respectively.

In a second approach, the off-stoichiometries of the films deposited within this thesis were evaluated according to the method described in Section 4.4. This method is based on the STM images of the sample surface before and after the growth. The respective results are shown in Figure 4.12(a), and comparing them with the results based on the XPS measurements (see Figure 4.11) it can be noticed that this method is significantly more accurate due to the smaller error bars. First, only the results corresponding to the regular samples are discussed (black data points). In order to model a mathematical relation between Δ_{Ti} and the laser fluence characterizing the growths, a distinction in cases is necessary.

As shown in Figure 4.12(a), films, which were grown using fluences below 2.05 J/cm^2, are characterized by negative values of Δ_{Ti} and therefore by an excess of Sr, which

is becoming more pronounced with decreasing laser fluence. In this context it has to be noted that Nb-doped films (full circles) and undoped films (hollowed circles) do not differ in terms of off-stoichiometries. As discussed in Section 4.3.2, the surfaces of the films grown using low laser fluences are determined by (4×1) and (5×1) reconstructions only, and more importantly there are no special features such as pits. Therefore, when applying the model of quantifying the off-stoichiometries via STM no additional assumptions have to be met, and subsequently the data points within this range are considered trustworthy. A possible explanation for Sr enrichment within PLD-grown films of STO is that Sr and Ti differ in their angular dispersions because of differences in the scattering processes with the background gas on their way from the target to the substrate [21]. Since Sr has a higher atomic mass compared to Ti the angular deviation of a Sr-atom scattering with a gas molecule is less compared to one of a Ti-atom in an equivalent event, resulting in a Sr-rich material flow towards the substrate. However, our experiments were characterized by such low pressures (3-7×10^{-6} mbar) that the corresponding mean free path exceeds the target-substrate distance, and thus such effects can be ruled out. The more plausible explanation for the Sr excess is that Sr is ablated preferentially when using low fluences, leaving a Ti-enriched target surface behind [14]. In order to maintain such an off-stoichiometric ablation over a long period, Sr has to diffuse from the bulk of the target surface to keep the gradient in the Sr concentration constant.

Films, which were grown using high fluences, in particular higher than 2.05 J/cm^2, are characterized by a slight excess of Ti, which is significantly less pronounced than the Sr excess of the films grown using low fluences, as shown in Figure 4.12(a). As already discussed in Section 4.3.1, when depositing material using high laser fluences, pits are formed as a result of the growth process. In the process of evaluating the off-stoichiometries, the pits were taken into account by assigning them to be (2×4) reconstructed, as shown in Figure 4.5. Nevertheless, within this range of laser fluence, more parameters are involved in the evaluation of the off-stoichiometries compared to the Sr-rich regime, and thus more possibilities of making systematic errors may occur. For example, it could be possible that a systematic mis-evaluation of the relative areal share of (2×4), A_P, causes the difference in slopes of the off-stoichiometries in the Ti-rich and Sr-rich regimes, as shown in Figure 4.12(a). In order to answer this question, the effect of a variation of A_P on Δ_{Ti} was studied based on Equation 4.3. The result was that even significant deviations in A_P, as much as 500 %, cannot describe the observed trend in the Ti-rich regime.

The off-stoichiometries that were derived by the method described in Section 4.4 using STM images are in accordance with the literature. Both Dam [14] and Ohnishi [12] measured a Sr excess in homoepitaxial films of STO, grown using low laser fluences. For high fluences however, Dam did not detect any off-stoichiometries whereas Ohnishi measured a slight Ti-excess, which was significantly lower compared to the Sr-excess of the films characterized by a low fluence. It is possible that such a small Ti-excess was within the error range of Dam's method (Rutherford backscattering spectroscopy). The most likely explanation for such a behaviour is that Sr is ablated preferentially using low laser fluences. Once a threshold fluence of 2.05 J/cm^2 is exceeded, the ablation process changes such that the deposited material becomes slightly Ti-rich. At this stage we cannot provide an explanation for such a behaviour.

Figure 4.12(b) shows the deposition rate as a function of the laser fluence. Similar to the off-stoichiometries, this quantity is also characterized by a kink at a threshold fluence of 2.05 J/cm^2, as indicated by the dashed lines. The same observation was made by Dam in their experiments [14], underlining the fact that the ablation process changes at a certain threshold fluence.

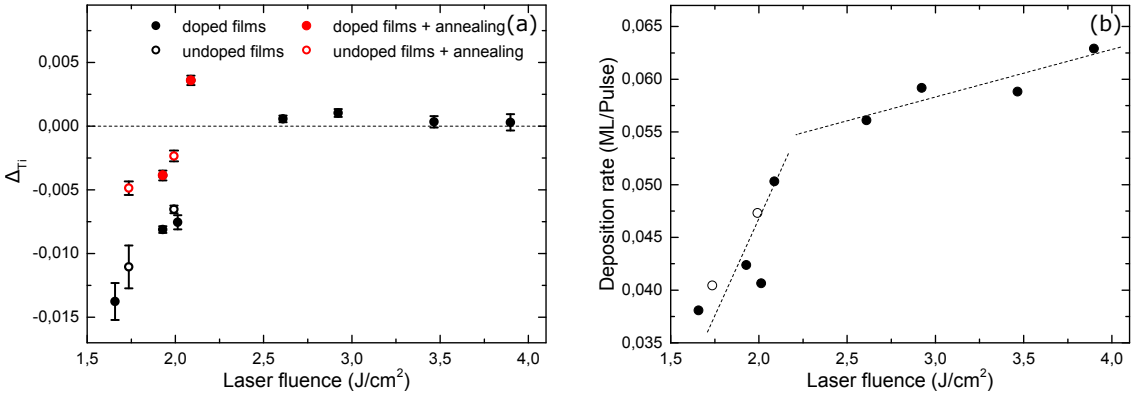

FIGURE 4.12: (a) Dimensionless Ti off-stoichiometry parameter Δ_{Ti}, as defined in 4.4, as a function of the laser fluence of the respective growths. The dashed line Δ_{Ti}=0 represents perfectly stoichiometric growth, whereas Δ_{Ti}>0 and Δ_{Ti}<0 indicate Ti-rich and Sr-rich growths, respectively. (b) Dependence of the deposition rate on the laser fluence. The dashed lines guide the eye in distinguishing between the low-fluence and the high-fluence regime.

The red data points in Figure 4.12(a) represent the off-stoichiometries of deposited films of STO, after an additional annealing for 4 h at 1000 °C (3-7×10^{-6} mbar oxygen environment) with respect to the corresponding substrates before the growth. By comparing these off-stoichiometries with the respective values before the annealing (black data points of the same fluence), one can see that they are shifted upwards

by a constant value of approximately 0.005, meaning that the surfaces becomes Ti-enriched.

There are two possible explanations for a Ti-enrichment of the surfaces of the films through an annealing processes at 1000 °C. Off-stoichiometries diffuse either from the bulk of the film or from the bulk of the substrate to the surface. In order to answer this question a reference experiment was performed, in which a (4×1)-(5×1)-prepared substrate was annealed for 4 h at 1000 °C in 3-7×10^{-6} mbar oxygen environment. The change in the surface stoichiometry was determined by the same procedure (see Section 4.4) as for the other samples,*i.e.*, by precisely evaluating the composition of the respective surface reconstructions in the small-scale STM images before and after annealing. For this bare substrate a Ti enrichment of the surface was determined characterized by the same magnitude as the shift in Δ_{Ti} through the annealings of films. It can thus be concluded that bulk diffusion processes from the substrate account for the change in stoichiometry during annealing of the PLD-grown films at 1000 °C.

5 CONCLUSION

The main achievements of this thesis comprise the successful growths by pulsed laser deposition of homoepitaxial $SrTiO_3$(110) thin films characterized by different fluences, and the development and application of a procedure to quantify off-stoichiometries within the films, based on scanning tunnelling microscopy images before and after the growths.

Commercially bought Nb-doped $SrTiO_3$(110) were prepared *in situ* by cycles of sputtering and annealing as well as submonolayer depositions of Sr and Ti followed by annealing, such that flat and well-ordered surfaces were obtained, with (4×1) and (5×1) reconstructions coexisting at the same time.

Such prepared samples were used as substrates for homoepitaxial growths of $SrTiO_3$(110) by means of pulsed laser deposition. The growths were characterized by a substrate temperature of 750 °C, 3-7×10^{-6} mbar oxygen environment, a target-substrate distance of 5.5 cm, and ablation laser fluences in the range from 1.66 J/cm^2 to 3.90 J/cm^2. The depositions were live-monitored by measuring the RHEED intensity of the specularly reflected beam. The signal was characterized by clear oscillations corresponding to the layer-by-layer growth mode, allowing to determine in real-time the number of deposited monolayers by counting the oscillations in the signal.

Scanning tunnelling microscopy analysis of the films revealed that their surface morphology depends on the fluence used for the deposition process. Films grown using low fluence are chararacterized by a flat surface terminated by (4×1) and (5×1), while the surfaces of films grown using high fluences consist of both flat (4×1)-(5×1)-reconstructed parts, as well as (2×4)-reconstructed pits.

During this thesis an STM-based method was developed to precisely evaluate the off-stoichiometries. Based on the assumption that the films grow stoichiometrically in the bulk and all the off-stoichiometries accumulate on their surface, this method can be used to precisely evaluate the changes of the composition of the respective surface

reconstructions, before and after the growths, and relating them to the information obtained in a reference experiment.

By means of this method it was shown that films grown using low laser fluences are characterized by a Sr-excess, which becomes more pronounced with a decrease in the fluence. Conversely, films grown using high fluences are characterized by a slight Ti-excess which, however, is significantly lower compared to the Sr-excess observed in the films grown using low fluences. X-ray photoelectron spectroscopy turned out to be not sensitive enough to detect the small changes in stoichiometry that were instead observed in scanning tunnelling microscopy.

Shortly after my thesis a key experiment strengthening the hypothesis that all the off-stoichiometries float to the surface was performed: $SrTiO_3$(110) samples, which were ideally identically terminated, were used as substrates for the growth of homoepitaxial films of different thicknesses. The off-stoichiometries in the films were then measured via the method based on the scanning tunnelling microscopy images and a linear dependence on the thickness, without an offset, was observed. Such a behaviour is expected if the bulk of the films grow stoichiometric and all the off-stoichiometries accumulate at their surfaces.

Since the approach of quantifying off-stoichiometries using scanning tunnelling microscopy images is based on an idealized model described within this thesis, it would be very interesting to apply it to homoepitaxial growths of other perovskite materials with a similar surface phase diagram as well.

List of Figures

Bibliography

[1] K. van Benthem, C. Elsässer, and R. H. French, "Bulk electronic structure of $SrTiO_3$: Experiment and theory," J. Appl. Phys. **90**, 6156 (2001).

[2] J. G. Mavroides, J. A. Kafalas, and D. F. Kolesar, "Photoelectrolysis of water in cells with $SrTiO_3$ anodes," Appl. Phys. Lett. **28**, 241 (1976).

[3] O. N. Tufte and P. W. Chapman, "Electron mobility in semiconducting strontium titanate," Phys. Rev. **155**, 796 (1967).

[4] F. Li, F. Yang, Y. Liang, S. Li, Z. Yang, Q. Zhang, W. Li, X. Zhu, L. Gu, J. Zhang, E. W. Plummer, and J. Guo, "δ-doping of oxygen vacancies dictated by thermodynamics in epitaxial $SrTiO_3$ films," AIP Adv. **7**, 065001 (2017).

[5] A. Ohtomo and H. Y. Hwang, "A high-mobility electron gas at the $LaAlO_3/SrTiO_3$ heterointerface," Nature **427**, 423 (2004).

[6] N. Reyren, S. Thiel, A. D. Caviglia, L. F. Kourkoutis, G. Hammerl, C. Richter, C. W. Schneider, T. Kopp, A.-S. Rüetschi, D. Jaccard, M. Gabay, D. A. Muller, J.-M. Triscone, and J. Mannhart, "Superconducting interfaces between insulating oxides," Science **317**, 1196 (2007).

[7] C. Noguera, "Polar oxide surfaces," J. Phys.: Condens. Matter **12**, R367 (2000).

[8] Z. Wang, F. Yang, Z. Zhang, Y. Tang, J. Feng, K. Wu, Q. Guo, and J. Guo, "Evolution of the surface structures on $SrTiO_3(110)$ tuned by Ti or Sr concentration," Phys. Rev. B **83**, 155453 (2011).

[9] J. A. Enterkin, A. K. Subramanian, B. C. Russell, M. R. Castell, K. R. Poeppelmeier, and L. D. Marks, "A homologous series of structures on the surface of $SrTiO_3(110)$," Nat. Mater. **9**, 245 (2010).

[10] S. Gerhold, *Surface Reactivity and Homoepitaxial Growth of Strontium Titanate (110)*, Ph.D. thesis, Technische Universität Wien (2016).

[11] Z. Wang, J. Feng, Y. Yang, Y. Yao, L. Gu, F. Yang, Q. Guo, and J. Guo, "Cation stoichiometry optimization of $SrTiO_3$(110) thin films with atomic precision in homogeneous molecular beam epitaxy," Appl. Phys. Lett. **100**, 051602 (2012).

[12] T. Ohnishi, M. Lippmaa, T. Yamamoto, S. Meguro, and H. Koinuma, "Improved stoichiometry and misfit control in perovskite thin film formation at a critical fluence by pulsed laser deposition," Appl. Phys. Lett. **87**, 241919 (2005).

[13] H. M. Christen and G. Eres, "Recent advances in pulsed-laser deposition of complex oxides," J. Phys.: Condens. Matter **20**, 264005 (2008).

[14] B. Dam, J. H. Rector, J. Johansson, S. Kars, and R. Griessen, "Stoichiometric transfer of complex oxides by pulsed laser deposition," Appl. Surf. Sci. **96-98**, 679 (1996).

[15] C. Xu, S. Wicklein, A. Sambri, S. Amoruso, M. Moors, and R. Dittmann, "Impact of the interplay between nonstoichiometry and kinetic energy of the plume species on the growth mode of $SrTiO_3$ thin films," J. Phys. D: Appl. Phys. **47**, 034009 (2014).

[16] T. Ohnishi, K. Shibuya, T. Yamamoto, and M. Lippmaa, "Defects and transport in complex oxide thin films," J. Appl. Phys. **103**, 103703 (2008).

[17] "Scroll pump," pchemlabs.com/product.asp?pid=3102 (2014), accessed: 2018-02-05.

[18] "Turbomolecular pump," en.wikipedia.org/wiki/Turbomolecular_pump (2017), accessed: 2018-02-05.

[19] "Ion pump," pchemlabs.com/product.asp?pid=5757 (2014), accessed: 2018-02-05.

[20] S. Gerhold, M. Riva, B. Yildiz, M. Schmid, and U. Diebold, "Adjusting island density and morphology of the $SrTiO_3$(110)-(4×1) surface: Pulsed laser deposition combined with scanning tunneling microscopy," Surf. Sci. **651**, 76 (2016).

[21] R. Dittmann, "Stoichiometry in epitaxial oxide thin films," in *Epitaxial Growth of Complex Metal Oxides*, edited by G. Koster, M. Huijben, and G. Rijnders.